AN ABSTRACT OF THE THESIS OF

Manuela Peter for the degree of Master of Science in Physics presented on February 8, 1996.

Title:

Impact Excitation Efficiency in AC-Driven Thin-Film Electroluminescent Devices.

Abstract approved: Redacted for Privacy

Thomas K. Plant

For the further development of AC-driven thin-film electroluminescent (ACTFEL) devices it is necessary to have more accurate models of the electron transport and the excitation efficiency in these devices. The purpose of this thesis is the experimental assessment of the impact excitation efficiency with respect to the applied phosphor field in several types of ACTFEL devices. A field-control circuit is used for the maintenance and control of the phosphor field during the measurement. The experimental data obtained from these measurements can be used for the calibration of unknown parameters in high field transport Monte Carlo simulations. Two ACTFEL devices are investigated. The threshold internal electric field for impact excitation in an evaporated ZnS:Mn ACTFEL device operated at 300K is $\sim$ 1.3 MV/cm. At 52 K it reduces to $\sim$ 1.0 MV/cm. The onset of saturation occurs at $\sim$ 2.1 MV/cm for device operation at 52 K. At 300 K the impact excitation efficiency does not saturate up to fields of 2.2 MV/cm. The threshold field for a sputtered $CaSrGa_2S_4$: Ce ACTFEL device operated at 300 K is $\sim$ 1.4 MV/cm. The impact excitation efficiency does not saturate up to fields of 2.5 MV/cm.

The ZnS:Mn ACTFEL device impact excitation trends suggest that phonon-assisted tunneling from interface states plays a role in the electron injection properties of this device and that band-to-band impact ionization occurs at fields of ~ 2 MV/cm at low temperature (~ 56 K). In contrast, $CaSrGa_2S_4 : Ce$ ACTFEL device impact excitation trends indicate that phonon-assisted tunneling plays less of a role, if any, in the electron injection properties of this device and that there are two kinds of conduction charge mechanisms in this device. Additionally, a low-field prethreshold luminescence is measured at low temperature for the $CaSrGa_2S_4 : Ce$ ACTFEL device. The nature of this prethreshold luminescence is not precisely understood.

Impact Excitation Efficiency

in AC-Driven Thin-Film Electroluminescent Devices

by

Manuela Peter

A Thesis

submitted to

Oregon State University

in partial fulfillment of
the requirements for the
degree of

Master of Science

Completed February 8, 1996
Commencement June 1996

Master of Science thesis of Manuela Peter presented on February 8, 1996

APPROVED:

Redacted for Privacy

Major Professor, representing Physics

Redacted for Privacy

Chair of the Department of Physics

Redacted for Privacy

Dean of the Graduate School

I understand that my thesis will become part of the permanent collection of Oregon State University libraries. My signature below authorizes release of my thesis to any reader upon request.

Redacted for Privacy

Manuela Peter, Author

ACKNOWLEDGMENT

I would like to thank Professor Gerd Haeusler for his encouragement to pursue graduate studies in the US and Professor Thomas K. Plant for providing me with the thesis topic and for serving as my advisor. I owe special gratitude to Professor John F. Wager for his guidance during the course of research and thesis preparation. His support, encouragement, and patience contributed essentially to my professional growth. I am grateful to Kevin Lite for many useful discussions and his help in the laboratory. My appreciation also to Professors Clifford Fairchild, William Hetherington, and Don Solmon for serving on my committee.

This work was supported by the U.S. Army Research Office under contract DAAH04-94-G-0324 and by the Advanced Research Projects Agency under the Phosphor Technology Center of Excellence, Grant No. MDA 972-91-1-0030.

TABLE OF CONTENTS

TABLE OF CONTENTS (Continued)

LIST OF FIGURES

LIST OF FIGURES (Continued)

Figure | Page

LIST OF FIGURES (Continued)

IMPACT EXCITATION EFFICIENCY IN AC-DRIVEN THIN-FILM ELECTROLUMINESCENT DEVICES

1. INTRODUCTION

In the last decade a demand for flat panel displays has emerged. Part of this demand is related to the development of new technologies such as high definition television, heads-up displays, and virtual reality. Conventional cathode ray tubes are currently being replaced by flat panel displays. Liquid crystal displays, plasma displays and electroluminescent (EL) displays are presently the dominant flat panel display implementations.

EL displays are believed to be promising because of their high brightness, wide viewing angle, high contrast, physical ruggedness, wide range of operating temperatures, and emissive nature. "Electroluminescence (EL) is a nonthermal generation of light resulting from the application of an electric field to a substance" [1]. It was discovered in 1936, when the French physicist Destriau observed light emission from a ZnS phosphor powder sandwiched between two electrodes. However, no effort was made to develop practical devices until the 1950's when electrically conductive films made of SnO_2 were developed.

During the late 1950's to the early 1960's worldwide research focused on flat light sources for wall illumination. With the development of yellow-emitting ZnS:Mn thin-film devices which yielded a much larger increase in brightness with applied voltage than earlier ZnS:Mn powder devices, EL devices finally held promise

for matrix-addressed displays. However, the reliability of these early ZnS:Mn thin-film EL displays was poor. The EL display reliability was greatly improved in 1967 by Russ and Kennedy when they introduced a double insulating-layer type AC thin-film EL (ACTFEL) structure, [1]. This is the basic structure used today in commercial thin-film EL displays.

The main goal today is to produce full-color thin-film EL displays. This requires phosphor materials that emit the three primary colors: red, green, and blue. Many studies have been directed to find suitable combinations of new EL host materials and luminescent centers. Most efforts were concerned with ZnS host materials doped with rare-earth luminescent centers. SrS and CaS have also been employed successfully as host materials, using europium and cerium as luminescent impurities. Recently, a new class of blue-emitting thin-film EL devices based on alkaline-earth thiogallates has been developed. In particular, $CaSrGa_2S_4$: Ce emits deep blue with a luminescence close to that required for practical displays. In 1993 a prototype 10-inch-diagonal 640 x 480 pixel full-color display was developed using a dual substrate EL panel structure [1]. The first commercial full-color thin-film EL display monitor with 320 x 256 pixels was introduced into the market in 1994, [1].

For further improvement of EL displays it is important to understand the underlying physics of these devices. Some key issues are the hot electron distribution and the interface state density distribution. Knowledge of these distributions is necessary for the development of accurate device models and simulations of the display performance. The electron transport physics of EL devices is still a matter of controversy.

The goal of this thesis is to experimentally assess the dependence of the conduction charge on the phosphor field and its efficiency in exciting electroluminescent impurities. Since impact excitation is believed to be the dominant luminescent

impurity excitation mechanism, an impact excitation efficiency is determined. Experimental assessment of the hot electron distribution has already been published by Krupka [2] and Streicher [3] for green ZnS : Tb ACTFEL devices.

The work reported herein replicates and expands Streicher's work by measuring the impact excitation quantum efficiency of yellow ZnS:Mn and blue $CaSrGa_2S_4$: Ce ACTFEL devices. The attainment of a constant phosphor field is a very subtle part of the experiment and is considered in more detail in this thesis than in previous work [4, 5]. Also, an extensive modification of the cryostat allows for measurements at lower temperatures than reported previously [3], and software development automation allows processing of the collected data more efficiently.

The thesis is organized in the following manner. Chapter 2 reviews relevant literature. Chapter 3 presents the background of standard experimental techniques relevant to this thesis. The experimental assessment of the quantum efficiency is described in Chapter 4. Experimental results are presented and discussed in Chapter 5. Chapter 6 then presents conclusions and suggestions for further research.

2. THEORETICAL BACKGROUND

In this chapter the theoretical background is established for the electrical and optical ACTFEL characterization techniques employed in this thesis. The device structure and operation are first reviewed. Establishment of the electrical background begins with a derivation of the electrostatic equations for the internal charge density and the phosphor field. These equations are used for the assessment of measurable quantities, as discussed in Chapter 4. Next the dynamic phosphor field equation is developed. This dynamic field equation is of fundamental importance in the development of a calibration procedure for the field control circuit, as discussed in Chapter 4. Three subsequent subsections focus on the internal current. Also carrier sourcing and electron transport in the phosphor are considered. Finally, excitation and light emitting mechanisms for electroluminescent centers are discussed and a definition of the impact excitation quantum yield, η_{ie}, is given.

2.1. ACTFEL Device Structure and Operation

The double-insulating layer type of ACTFEL devices is shown in Fig. 2.1. The phosphor is sandwiched between two transparent insulator layers and a pair of electrodes. The glass-side electrode is usually indium-tin oxide (ITO) which is transparent and permits viewing of the emitted light through the glass substrate. The other electrode is aluminum. The insulators are typically silicon oxi-nitride (SiON), barium tantalate (BTO), or aluminum-titanium oxide (ATO). The central layer is the thin phosphor layer which emits light when a large enough electric field is applied across it. This field is of the order of 1-3 MV/cm. The insulating layers

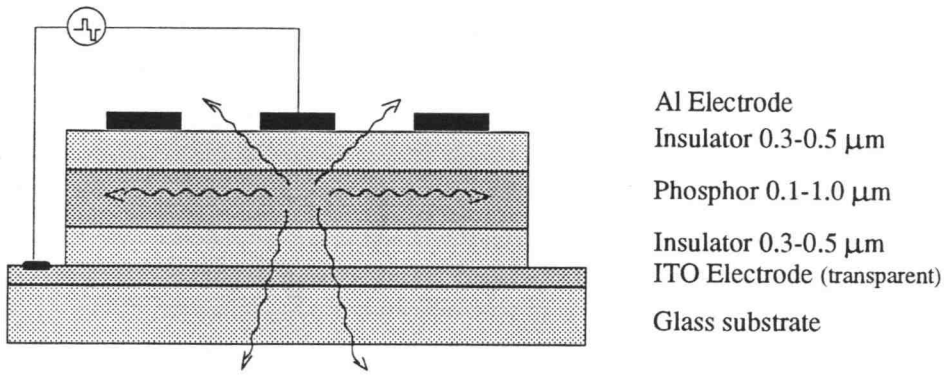

FIGURE 2.1. Typical ACTFEL device structure.

preclude the flow of drift current so that the ACTFEL device is capacitively coupled (i.e. only displacement current is important in the insulators). Thus, direct electron flow from the electrodes to the phosphor layer is prevented. Without the insulating layers, any imperfection in the thin-film phosphor that produces a short circuit would cause a destructive breakdown of the phosphor. The insulating layers result in a high break down field. The ACTFEL device operates by the application of a large AC voltage across the external electrodes. The total externally applied voltage is then capacitively divided across the two insulating layers and the phosphor layer. The voltage waveform is often of a rectangular shape with short rise and fall times. The maximum applied voltage is usually 30 to 60 V above the threshold voltage of the device. The electron emission mechanism is indicated in Fig. 2.2. At high fields, electrons are injected from interface states via field-assisted tunneling. The injected electrons are accelerated by the field and can excite luminescent impurities, if they gain enough kinetic energy. High-energy electrons, also called hot electrons,

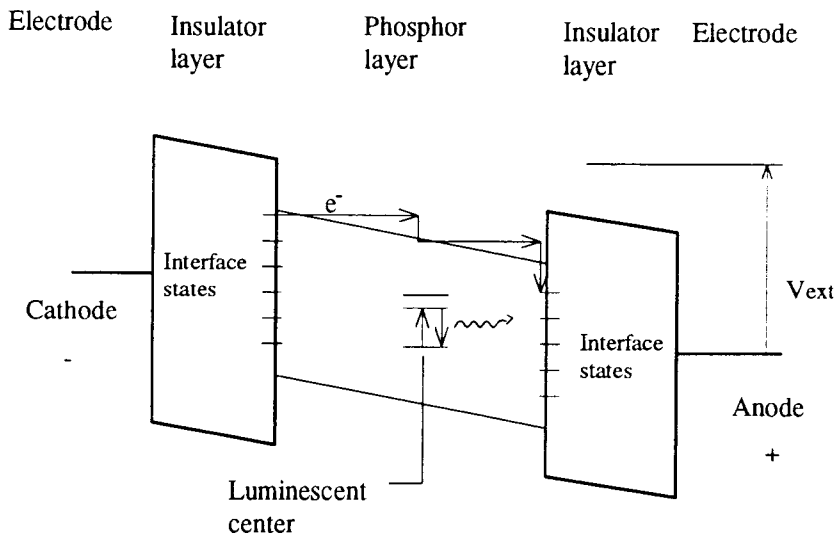

FIGURE 2.2. Energy band diagram of the double insulating layer type ACTFEL device.

excite luminescent impurities directly through impact-excitation. The luminescent impurity can then return to its ground state via light emission or by nonradiative relaxation in which the decay energy is dissipated in the lattice as phonons. The hot electrons are finally trapped at the interface on the anode side and give rise to polarization of the phosphor layer. The same process takes place in the reverse direction during the inverse polarity of the AC voltage waveform. Since tunnel injection is temperature insensitive, ACTFEL devices can be used over a wide range of temperature (from 10 K to 500 K !).

2.2. ACTFEL Device Modeling

2.2.1. Electrostatics

The aim of this section is to derive the electrostatic equations for the phosphor field, f_p, and for the internal charge transfer per unit area in the phosphor, q_{int}, and to relate these internal quantities to externally measurable quantities. The externally measurable quantities are the applied voltage, v_{ext}, and the charge density at the electrodes, q_{ext}.

Several models have been developed to describe the ACTFEL device behavior. Bringuier's model [6] is employed in the following discussion, with particular emphasis on the electrical properties. The ACTFEL device is modeled as a multilayer capacitor where the phosphor is the central layer. In order to relate internal features of the device to externally measurable quantities the following assumptions are made:

- The dielectric constants, ϵ_i, and thicknesses of both insulating layers are equal.
- The film thickness is uniform.
- The insulator layers, sandwiching the phosphor, are perfectly insulating at all fields.
- The mechanism of carrier emission is tunneling of electrons from the insulator-phosphor interface.
- A large density of partially filled deep levels exists at the insulator-phosphor interfaces.
- The fields across the layers are constant; that is, no space charge is present.

- No carrier multiplication occurs in the phosphor layer.

First, an equation for the phosphor field is derived in terms of v_{ext} and q_{ext}. According to Kirchhoff's voltage law, the externally applied voltage, v_{ext}, is the sum of the voltages across the insulator and phosphor layers of the ACTFEL device. With the assumption of uniform layer thicknesses, the phosphor field can be introduced

$$v_{ext} = v_i - f_p d_p. \tag{2.1}$$

Where d_p is the thickness of the phosphor layer and v_i is the total voltage drop across both insulator layers. The voltage across the insulator layers arises from the charge accumulated at the external electrodes. Hence the voltage across the insulator can be expressed in terms of the external charge density and the insulator capacitance per unit area, c_i, as

$$v_i = \frac{q_{ext}}{c_i}. \tag{2.2}$$

Substitution of Eqn. (2.2) in Eqn. (2.1) and rearranging leads to the phosphor field equation in terms of v_{ext} and q_{ext}

$$Phosphor\ Field\ Equation: \qquad f_p = -\frac{1}{d_p}(v_{ext} - \frac{q_{ext}}{c_i}). \tag{2.3}$$

Second, an equation for the density of transferred charge, q_{int}, at the phophor-insulator interfaces is derived. During device operation, two voltage regimes exist. For voltages below threshold voltage, v_{th}, the phosphor layer is insulating, no steady state conduction takes place in the phosphor. The phosphor layer is only capacitively coupled to the external circuit. In this case the externally applied charge density is too small to cause a strong enough field to separate charges in the phosphor.

$$|v_{ext}| < |v_{th}|: \qquad q_{int} = 0 \tag{2.4}$$

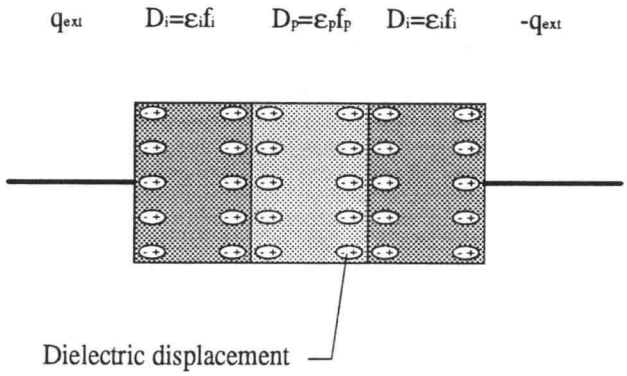

FIGURE 2.3. Dielectric film as a capacitor stack.

For voltages below $|v_{ext}|$ the electric flux density, $D = \epsilon f$, is continous and constant across the capacitor stack (thin-film). The external charge density equals the electric displacement, Fig. 2.3.

$$|v_{ext}| < |v_{th}| : \qquad q_{ext} = \epsilon_i f_i = \epsilon_p f_p = c_t v_{ext}, \tag{2.5}$$

Where ϵ_p is the phosphor dielectric constant, f_i is the electric field across each identical insulator and c_t is the total device capacitance. For voltages above threshold, the phosphor field is strong enough to free electrons from deep interface levels at the phosphor-insulator interface, Fig. 2.2. These electrons are then swept away by the electric field established in the phosphor and are accumulated at the anodic interface. If q_{int} is the positive charge per unit area left at one interface, then a negative charge density, $-q_{int}$, is accumulated at the opposite interface. The phosphor electric flux density, $D_p = \epsilon_p f_p$, is determined by the external charge at the electrodes plus the internal transferred charge accumulated at the interfaces, Fig. 2.4, which leads to

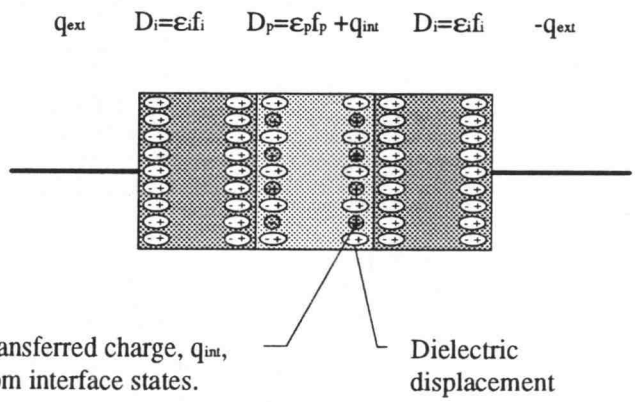

FIGURE 2.4. Charge accumulation in the capacitor stack.

$$|v_{th}| < |v_{ext}| \qquad \epsilon_p f_p = q_{ext} - q_{int}. \tag{2.6}$$

Using the definition of the capacitance per unit area in terms of the dielectric constant, $c_p = \epsilon_p / d_p$ and combining and rearranging Eqns. (2.3) and (2.6) results in

$$Internal\,Charge\,Density: \qquad q_{int} = c_p \left(\frac{q_{ext}}{c_t} - v_{ext} \right). \tag{2.7}$$

In equation (2.7) the relation between the total capacitance, the insulator capacitance, and the phosphor capacitance, $c_t = \frac{c_i c_p}{c_i + c_p}$, is already employed. The external charge density, q_{ext}, at the initially anodic electrode is a measurable quantity which may be monitored as the voltage across a sense capacitor connected in series to the ACTFEL device. The external charge is the sum of total displacement charge and the the internal transferred charge.

$$|v_{th}| < |v_{ext}|: \qquad q_{ext} = c_t v_{ext} + \frac{c_t}{c_p} q_{int} \tag{2.8}$$

Equation (2.7) is of fundamental importance. It establishes the internal charge density in terms of measurable quantities (i.e. v_{ext} and q_{ext}) and fundamental properties of the thin film layers (i.e. c_t and c_p).

The phosphor field and the internal charge density are not independent quantities. The accumulation of charge builds up a counter field which lowers the electric field in the phosphor and results concomitantly in a lower emission rate of electrons from interface states.

2.2.2. Dynamic Phosphor Field Equation

In this section the time dependence of the phosphor field and its dependence on the internal charge transfer are derived. To reiterate, an ACTFEL device behaves very differently for applied voltages below and above the threshold voltage. Below threshold, the device behaves essentially like a capacitor; that is, no conduction current flows in the phosphor. Thus, the internal conduction current density, $j_{int} = 0$. The external current is simply the displacement current of the capacitor:

$$|v_{ext}| < |v_{th}| : \qquad j_{ext} = c_t \frac{dv_{ext}}{dt}. \tag{2.9}$$

Where j_{ext} is the external current density. Above threshold, the internal current can be found by measuring the external current density which is composed of the total displacement current of the device and the internal conduction current density in the phosphor,

$$|v_{th}| < |v_{ext}| : \qquad j_{ext} = c_t \frac{dv_{ext}}{dt} + \frac{c_t}{c_p} j_{int} \tag{2.10}$$

This equation is obtained by taking the time derivative of Eqn. (2.8).

In order to relate the phosphor field to v_{ext} and to q_{int}, the phosphor field, Eqn. (2.8) is substituted in Eqn. (2.3):

$$f_p = -\frac{1}{d_p}\frac{1}{c_i + c_p}\left(c_i v_{ext} - q_{int}\right). \tag{2.11}$$

This is an electrostatic expression. To obtain a dynamic phosphor field, the time derivative of Eqn. (2.11) is taken. The time derivative of the internal charge density is transformed into the internal current density which leads to:

Dynamic

Phosphor Field Equation :
$$\frac{df_p}{dt} = -\frac{1}{d_p}\frac{1}{c_i + c_p}\left(c_i\frac{dv_{ext}}{dt} - j_{int}\right) \tag{2.12}$$

The phosphor field feedback effect is accounted for quantitatively in the dynamic phosphor field equation, Eqn. (2.12). The dynamic behavior of the phosphor field is governed by the displacement current and the conduction current in the phosphor. The phosphor field determines the amount of transferred charge which in turn modifies the phosphor field.

The conduction current depends very much on the internal features of the device, i.e. the interface state density distribution and occupation, the electron emission rate, and the possibility of carrier multiplication in the phosphor. Thus, the internal conduction current can provide information related to the internal device properties.

2.2.3. Carrier Sourcing from Interface States

The dynamic phosphor field equation establishes the connection between the phosphor field and the internal charge transfer, assuming all of the charge is sourced and sunk at the interfaces and that no carrier multiplication occurs in the phosphor. Further understanding of the details of the charge sourcing and the possibility of charge multiplication requires the use of specific models to account for trends in the experimental data.

The electric field adjacent to the interface of interest, the energy depth of the interface states, the capture cross section of the interface states, and the ambient temperature determine the emission rate of electrons from the insulator - phosphor interface. At low phosphor fields (less than about 1MV/cm), phonon assisted tunneling of electrons is believed [7] to be the dominant mechanism of carrier emission. At high fields (greater than about 1MV/cm), the dominant mechanism for electron emission from the interface states into the conduction band of the phosphor is by pure tunnel injection of electrons.

The model, developed by Bringuier, accounts for many of the characteristics found in ZnS ACTFEL devices [6], [8]. The model focuses on electrons being sourced from interface states. No other carrier sourcing is assumed and the possibility of carrier multiplication is not considered. The interfaces states are emptied via tunneling to the conduction band, Fig. 2.2. Therefore, within the assumptions of this model, the internal current density is dominated by the interface state density and its occupancy. To date, no reliable experimental determination of the interface state density has been made.

Bringuier performed simulations for two interface state density distributions, a discrete trap and a uniform density of traps. In the case of the discrete trap model, quasi-field clamping is predicted. That is, the phosphor field reaches a relatively constant maximum value when the internal current reaches a maximum. This quasi-field-clamping comes about when the transferred charge establishes a counterfield to that introduced externally, hindering the further transfer of charge. Since the internal current depends on the slew rate of the externally applied voltage, Eqn. (2.10), the maximum phosphor field depends on the shape of the applied voltage pulse. Note that a situation in which the phosphor field is relatively constant while the external applied voltage is increasing is referred to as "quasi-field-clamping".

"Field-clamping" is reserved for a situation in which the phosphor field is constant at the same value, independent of the maximum applied voltage of the applied voltage pulse [9].

Many ACTFEL devices do not exhibit quasi-field-clamping [6, 10, 11]. These cases may be accounted for by a low density of interface states. Alternatively, space charge generation in the phosphor layer can also lead to a situation in which quasi-field-clamping does not occur. Bringuier showed that quasi-field-clamping only occurs in cases of a high density of interface states and a quasi-Fermi level close to the conduction band. In such cases, the interface state distribution does not seem to matter very much; the device behavior appears to be dominated by the negative feedback associated with the transferred charge. In this case the discrete trap model can meaningfully be applied. For the case of a low density of interface states, quasi-field-clamping does not occur.

2.2.4. Hot Electron Distribution

This section addresses the hot electron distribution and establishes, together with the section on the luminous efficiency, the basis for the interpretation of the final quantum yield results. The electrons sourced from interface states are accelerated by the phosphor field. How efficiently they excite luminescent impurities depends on their energy distribution. The electron distribution is determined by the field heating and various counteracting loss mechanisms which are described in this section. Some models of the hot electron distributions and their predictions are presented.

The electrons freed from the interfaces, through field-induced tunneling or phonon assisted tunneling, gain energy from the applied phosphor field. This energy gain is counteracted by the properties of the solid. The simple presence of the

bulk is an ensemble of obstacles for the electrons to overcome. The electrons can be scattered by phonons or impact on a luminescent impurity, a bulk trap, or on a phosphor atom. High energy electrons can be scattered by either energetic acoustic or optical phonons. These electrons can impact excite the luminescent impurities and lose energy through the impact. If the excited states of the luminescent centers lie close to the conduction band in terms of the energy band diagram, then an ionization of the luminescent centers can occur as well. However, not only impacts with the luminescent centers can lead to energy loss, bulk traps in the lattice may also be impact excited by the hot electrons or ionized if their energy levels lie close enough to the conduction band to allow the ionization. Impact ionization of luminescent centers and bulk traps causes localized positive charges in the lattice which distort the phosphor field locally. If the kinetic energy of the electrons is sufficient to excite electrons from the valence band to the conduction band (band-to-band impact ionization), then no localized space charge develops and the created hole and conduction electron drift to the cathode and anode, respectively, contributing to the conduction charge. Thus, the energy loss of the hot electrons due to the inelastic scattering impedes a further heating of the "hot electron" energy distribution.

In modeling the energy distribution of electrons, two different approaches have been used: Monte Carlo simulation and Lucky-Drift modeling. In Monte Carlo simulation, the time evolution of a single carrier is considered, whereas in the Lucky-Drift picture, all the transport-related information is combined into an electron mean-free path parameter.

Brennan [12], 1988, conducted Monte Carlo simulations of ZnS host material and found that only about 1% of the transiting electrons reach energies beyond 2.12 eV, the Mn impact excitation threshold, at a phosphor field of 1 MV/cm. This small fraction could not explain why ZnS:Mn is a relatively efficient phosphor.

In 1990, Fitting, Mach and Mueller's Monte Carlo simulations, [13, 14] showed that a large number of hot electrons are supplied by ballistic acceleration.

Bringuier, in 1992, used the analytical Lucky-Drift model and found a value in between the two previous results. According to his calculation about 27% of the electrons exceeded the energy of 2.12 eV. This result was almost matched by results from Monte Carlo simulations conducted in 1993 by Bhattacharyya et al. [15] who found a value of about 26%. Pennathur [16] refined Bhattacharyya's model and found that about 18% of the electrons possess energies above 2.1 eV.

This variety of modeling results is due to the different assumptions made in the various models. Brennan used an empirical pseudo-potential band structure and a full-band structure calculation for the first two conduction bands plus electron-phonon scattering as a loss mechanism. Mach and Mueller assumed a single parabolic band structure and only polar optical-phonon scattering as a loss mechanism. Bhattacharyya et al. used a non-parabolic, multivalley model, and as loss mechanisms, electron scattering due to polar optical phonons and acoustic phonons, as well as intervalley scattering and ionized- and neutral-impurity scattering.

The latest model by Pennathur is a refinement of Bhattacharyya et al.'s model. Here the non-parabolic band was replaced by a full-band energy dispersion relation, which accounts for a lower density of higher energy states in the conduction band. Apart from the scattering at neutral impurities, all the electron scattering mechanisms from Bhattacharyya's model were included plus band-to-band impact ionization and impact excitation of the manganese impurities. Pennathur's Monte Carlo simulations showed that impact excitation processes do not affect the hot electron distribution to a significant degree. Increasing phosphor fields result in hotter energy distributions and the estimated internal quantum yield was found to vary linearly with the phosphor field. However, band-to-band impact ionization was

found to play a crucial role in stabilizing the electron distributions. That is, as soon as electrons gain energies sufficient for impact ionization, about 4.3 eV, the distribution does not significantly heat further due to the energy loss associated with the ionization process. Thus, the impact excitation efficiency is found to saturate in Pennathur's Monte Carlo simulations, as was observed by Streicher [5] in ZnS:Tb devices.

2.3. Luminescent Impurities

The goal of this thesis is to assess the hot-electron impact excitation efficiency of ACTFEL devices. However, only the total conversion efficiency of the electric input into the light output can be measured and the excitation efficiency, η_{exc}, [18] is only one part of the total conversion efficiency. The total conversion efficiency is a product of the excitation efficiency, η_{exc}, the luminescent efficiency, η_{lum}, and the light outcoupling efficiency, η_{out},

$$\eta = \eta_{exc}\eta_{lum}\eta_{out}. \tag{2.13}$$

The excitation efficiency is not easily extracted from the other efficiencies. Thus, this section is a review of the physical processes involved in the excitation and de-excitation of the luminescent impurities and the outcoupling of the resulting light.

2.3.1. Excitation Efficiency

Light emission in an electroluminescent device originates from the radiative decay of luminescent impurities embedded in the host lattice. The d- or f- shell

electrons of the luminescent impurities can be excited by direct field emission, by impact excitation, or by impact ionization via energetic electrons.

If an inelastic collision with a conduction electron takes place, the impurity can either be left in an excited state or be ionized. The first case is referred to as impact excitation, the latter as impact ionization. Whether impact excitation or ionization is dominant depends on the position of the excited state level of the luminescent impurity with respect to the conduction band edge. In the case of impact ionization, the center is ready to capture another conduction electron. This capture can be either radiative or nonradiative.

Experimental discrimination of which excitation mechanism prevails relies on assessing differences between the two mechanisms. Impact ionization has a time delay associated with the time it takes to capture a conduction electron. In contrast, impact excitation has no such time delay. Additionally, impact ionization supplies new carriers to the conduction band which can also be accelerated in the phosphor field and impact excite other luminescent centers. This ionization results in dynamic space charge generation which can be monitored via C-V or Q-V measurements (Section 3). Thus, a good way to determine whether impact ionization or impact excitation prevails is to examine the doping dependence of dynamic space charge. The dimensionless excitation yield is defined as:

$$\eta_{ie} \equiv \frac{Number\,of\,Excited\,Centers}{Number\,of\,Transferred\,Electrons} = \frac{N^*}{\frac{\Delta Q}{q}}. \tag{2.14}$$

Because no evidence for space charge generation has been found in the ZnS:Mn and $CaSrGa_2S_4$: Ce devices under investigation, it is assumed that no impact ionization of the luminescent impurities takes place. Hence, the excitation of luminescent impurities is attributed to impact excitation only. The excitation efficiency is therefore termed impact excitation efficiency.

2.3.2. Luminous Efficiency

De-excitation of a luminescent impurity does not necessarily result in radiative recombination. The excited luminescent impurity may return to its ground state via a radiative or a nonradiative mechanism. This prevents direct measurement of the excitation efficiency.

The return from the excited state to the ground state does not necessarily have to be radiative. If the temperature is high enough, the relaxed-exited state may lie close to the crossing between the ground state vibration energy parabola and the excited state parabola in the configuration diagram. The electron can then decay into a high vibrational level of the ground state and relax non-radiatively from there. The decay rate depends on the wave function overlap of the two vibrational levels. This model accounts for thermal quenching of luminescence.

Besides the nonradiative return to ground state, there is the possibility of interacting luminescent impurities transferring energy from one to another. It is possible that the excited state energy may be transferred to many other luminescent impurities prior to the final impurity radiatively or nonradiatively decaying. If the receptive center decays nonradiatively it is said to quench the emission. If the excitation energy usually reaches sites where it is lost nonradiatively, then the luminescence efficiency at that composition will be low. This type of quenching will only take place when the distance between the centers is small enough for the energy migration to readily occur, that is, if the dopant concentration is high enough.

Therefore, the luminescence decay time, τ, can depend strongly upon the dopant concentration [18] and may be given by,

$$\tau = \left(\frac{1}{\tau_r} + \frac{1}{\tau_{nr}(N)} \right)^{-1}, \tag{2.15}$$

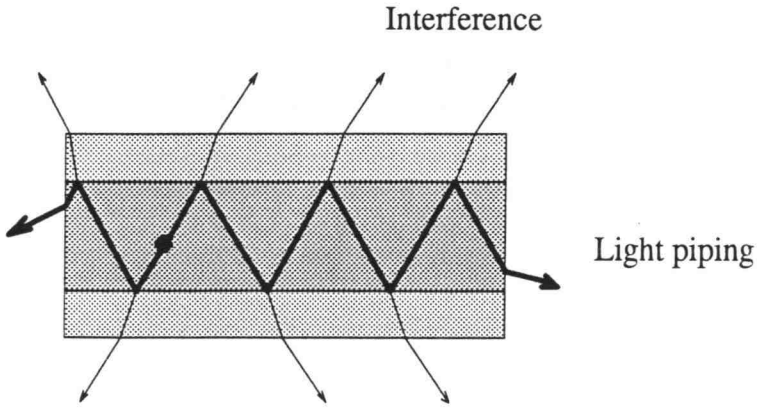

FIGURE 2.5. Optical outcoupling

Where τ_r is the time constant for radiative decay and τ_{nr} is the time constant for nonradiative decay. Note that the nonradiative decay time is explicitly shown to be dependent on the luminescent impurity doping density.
The luminescence yield is then defined as:

$$\eta_{lum}(N) = \frac{\tau(N)}{\tau_r} \tag{2.16}$$

The nonradiative decay will in general depend on the temperature and the number of luminescent impurities.

2.3.3. Outcoupling Efficiency

The outcoupling of photons generated in a phosphor with a thickness of the order of the wavelength of the emitted light leads inevitably to interference which causes a strong angular dependence of the spectral intensity. Since the thin phosphor

layer is usually of higher refractive index than the adjacent insulator layers, the outcoupling efficiency is seriously influenced by total internal reflection.

The outcoupling efficiency is not known for the devices investigated in this thesis. Thus, the outcoupling efficiency can not be separated from the total conversion efficiency. However, it is assumed that the outcoupling efficiency is independent of the temperature and the driving waveform. The lack of information on the outcoupling efficiency restricts the experimentally assessed excitation efficiency to be qualitative only.

Even though the outcoupling efficiency is disregarded, the measured conversion efficiency is still a product of the interlinked impact excitation efficiency and the luminous efficiency. With the assumption that the luminous efficiency is strongly temperature dependent, an estimate can then be given how strongly the measured conversion efficiency resembles to the impact excitation efficiency.

2.3.4. Manganese and Cerium

The primary luminescent impurities of interest in this thesis are the divalent transition metal ion Mn and the trivalent rare earth ion Ce. The crystal field effect for transition metals ions, which have partially filled d shells, is much larger than for rare earth ions, which have partially filled f shells.

2.3.4.1. Transition Metal Ion: Manganese

Manganese has the electron configuration: $[Ar]3d^5 4s^2$. Mn^{2+}, $[Ar]3d^5$, has a broad emission band whose position depends strongly on the host lattice. The emission color depends on the host crystal field and can vary from green to deep red. The long decay time of Mn^{2+}, of the order of milliseconds, is due to the forbidden

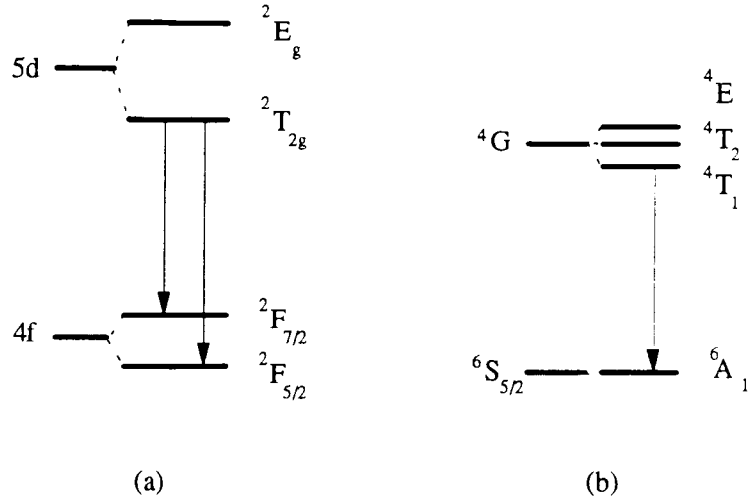

FIGURE 2.6. Simplified energy level scheme of the Ce^{3+} ion, (a), and the Mn^{2+} ion, (b).

nature of the spin selection rule. A simplified energy level scheme of Mn^{2+} in ZnS is shown in Fig. 2.6, [19]. The $3d^5$ level splits into several levels, ^{6}S,^{4}G,^{4}F,^{4}D..., due to interelectronic repulsion. The levels split further due to the host crystal field. The luminescence occurs from the $^4T_1$ to the $^6A_1$ level.

2.3.4.2. Rare Earth Ion: Cerium

Rare earth ions have incompletely filled $4f$ shells. The $4f$ orbital is an inner core shell which is sheltered from the surrounding crystal lattice atoms by the outer filled $5s^2$, $5p^6$ and $6s^2$ orbitals. The influence of the host lattice on the optical transitions within the $4f^n$ configuration is small and the color of the luminescence is not strongly affected by the crystal lattice of the host. Several rare earth ions show

broad band emission. In this type of emission an electron returns from a $5d$ orbital to a $4f$ orbital [20] instead of the more common $4f \rightarrow 4f$ transitions. The $5d$ to $4f$ transition is fully allowed and the decay time is therefore very short, typically on the order of nanoseconds.

Ce has the electron configuration $[Xe]4f^15d^16s^2$. The Ce^{3+} ion, $[Xe]4f^1$, is the simplest example since it is a case in which there is one electron in the f-shell. The excited state configuration is $5d^1$. The host lattice crystal field splits the excited configuration into 2 to 5 components. The $4f^1$ ground state configuration yields two levels, $^2F_{\frac{5}{2}}$ and $^2F_{\frac{7}{2}}$, which are separated by some 2000 cm^{-1} due to spin-orbit coupling. This splitting results in the characteristic spectrum of cerium. Emission takes place from the lowest crystal field component in the excited configuration to the two ground state levels. [21] The decay time of the Ce^{3+} emission is short, $\sim 10^{-8}s$. The Ce^{3+} emission is usually in the ultraviolet or blue region, but crystal field effects can shift it to the red.

3. STANDARD EXPERIMENTAL TECHNIQUES

There are several techniques that were developed for the electrical characterization of ACTFEL devices to allow for the assessment of the insulator capacitance and to investigate space charge behavior. In the following section, two techniques are described which are commonly used for the assessment of the insulator capacitance of an ACTFEL device. They are termed charge-voltage (Q-V) and capacitance-voltage (C-V) measurement techniques. Both techniques are based on the previously described multilayer capacitor model. This model provides equations for the assessment of the internal phosphor field and internal polarization charge. Thus, polarization charge, leakage charge, relaxation charge, and the steady-state phosphor field can be assessed provided that no space charge is present and that the insulator and phosphor capacitances are known. Before the two measurement techniques are explained, the time response of an ACTFEL device to a rectangular waveform is treated in order to establish the terminology associated with the methods and to give a better understanding of the time response of the device to the applied voltage.

3.1. ACTFEL Response to a Trapezoidal AC Voltage Waveform

Figure (3.1) shows the applied bipolar trapezoidal voltage waveform in Q-V and C-V measurements, and the response of the ACTFEL device. If the applied voltage exceeds the threshold value, charge is sourced from the interfaces. The current flow then no longer consists only of the total displacement current of the capacitive stack but has a contribution from the charge injection of the interface states. Above threshold, point "B" in Fig. 3.1, during the rise time of the applied voltage,

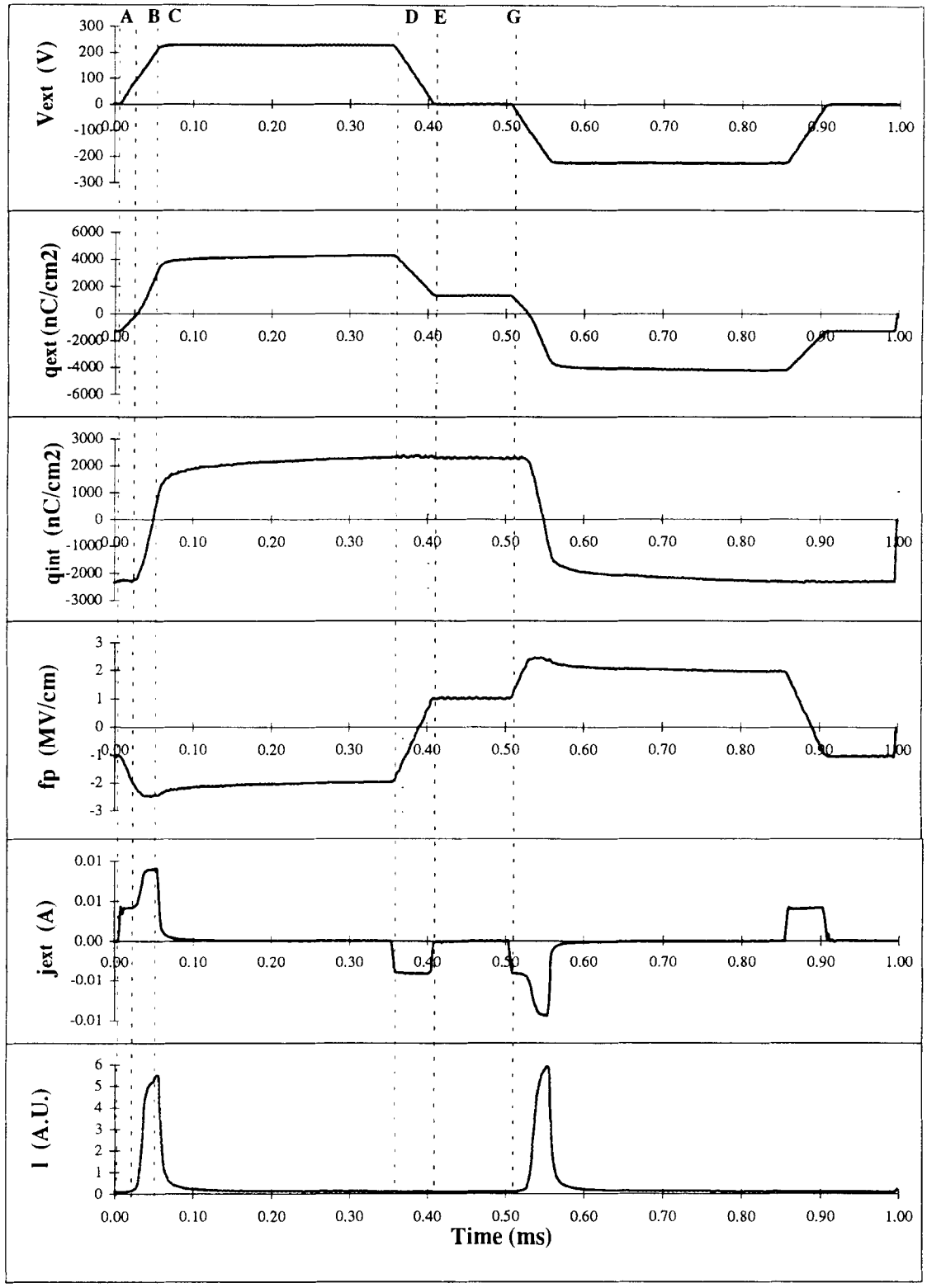

FIGURE 3.1. Time response of an ACTFEL $CaSrGa_2S_4$: Ce device to the applied voltage waveform.

the externally accumulated charge increases with a much steeper slope than below threshold due to the essentially shorted phosphor layer. The phosphor field increases during the augmentation of the external bias. As soon as the internal charge transfer takes place, polarization charge is accumulated on the opposite phosphor interface and the phosphor field increment diminishes due to this internal charge opposing the external bias. During the constant external bias,C to D in Fig. 3.1, the internal field relaxes due to the further charge transfer from the phosphor interfaces which adds to the counteracting internal polarization charge until the charge transfer and the field reduction balance each other. In the work described in this thesis, the phosphor field is held constant by means of a field control circuit, as described later in the experimental section. The charge transfer during the relaxation of the phosphor field is termed "relaxation charge". In the case that the phosphor field induced by the internal polarization charge is sufficiently strong, some transferred charge can leak back to its "original" interface during the falling edge of the positive voltage pulse, D to E. This charge is termed leakage charge. The remaining transferred charge, E to G, maintains an internal polarization of the phosphor until another voltage pulse of opposite polarity is applied and is termed "polarization charge". Luminescence is usually observed during the charge transfer portion of the rising edge of the driving waveform. In some devices, e.g. SrS:Ce, the leakage charge during the falling or trailing edge of the wave form can result in luminescence as well.

The external features of an ACTFEL device, i.e. external charge and displacement current, are measured across either a capacitor (see Fig. 3.2) or a resistor in series with the device. The capacitor allows the externally accumulated charge to be monitored directly while the resistor allows the total displacement current of the device to be measured directly. For both methods it is only the leading edge of

the (positive or negative) voltage pulse which is of interest for the estimation of the insulator capacitance.

3.2. Charge - Voltage (Q-V) Measurements

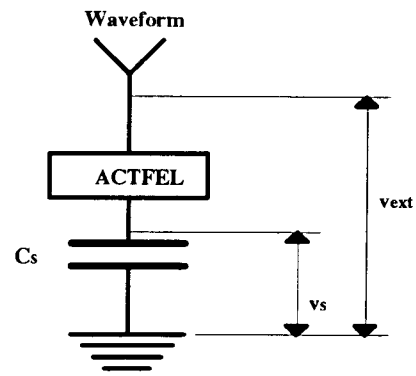

FIGURE 3.2. External charge monitoring.

The insulator and phosphor capacitances, C_i and C_p, may be found using the charge-voltage (Q-V) technique [5, 4]. Note that C is used to denote capacitance as opposed to capacitance per unit area, c, as introduced in Chapter 2. The charge-voltage technique monitors the external charge by means of a Sawyer-Tower configuration; that is, a sense capacitor is connected in series with the ACTFEL device. The external charge monitored by the sense capacitor is given by

$$Q_{ext} = C_s v_s. \tag{3.1}$$

Figure (3.3) shows the applied voltage waveform and the ideal Q-V curve for the positive half cycle of an ACTFEL device. For voltages below threshold, the ACTFEL device behaves like a multilayer capacitor so that the slope of a Q-V curve in this regime is equal to the total capacitance of the ACTFEL stack, C_t.

For applied voltages in excess of the threshold voltage, electrons are emitted from interface states and the phosphor layer is essentially shorted so that only the

insulator capacitance remains in the circuit shown in Fig. 3.4. The slope of the Q-V curve in this regime is ideally equal to the insulator capacitance, C_i. In practice, the Q-V slope above threshold is not always equal to the insulator capacitance since, for certain ACTFEL devices, the phosphor conduction current is not large enough that C_p can accurately assumed to be shorted, while other ACTFEL devices display space charge generation in the phosphor. The phosphor capacitance is then assessed

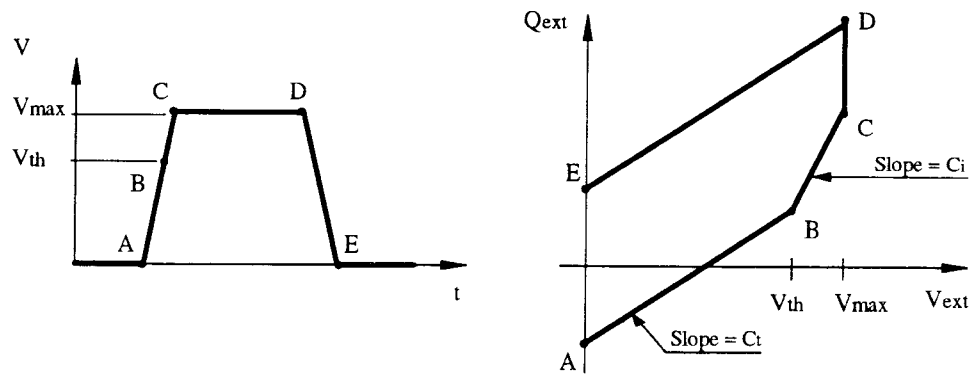

FIGURE 3.3. Applied voltage waveform and the resulting $Q_{ext} - V$ curve.

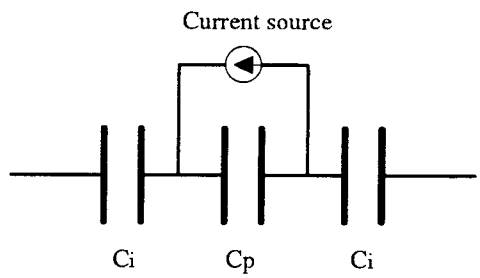

FIGURE 3.4. The ACTFEL device model above threshold.

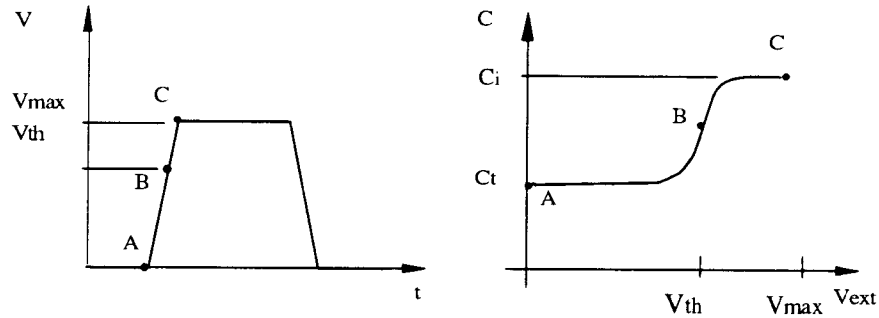

FIGURE 3.5. Applied voltage waveform and the resulting $C - V$ curve.

as a series combination of the capacitances of the phosphor and insulator layers,

$$C_t = \frac{C_i C_p}{C_i + C_p}. \tag{3.2}$$

3.3. Capacitance-Voltage (C-V) Measurements

Instead of measuring the slope of a Q-V curve, the external displacement current can be measured and the total capacitance of the ACTFEL device can then be calculated. In this case a resistor takes the place of the sense capacitor, and the voltage across the resistor is monitored in order to assess the external current. With the assumption that the insulators are perfectly insulating, only displacement current flows in the insulators. The total capacitance of the ACTFEL device is given by the ratio of the displacement current of the device to the rate of change of voltage across it,

$$C_t(v_{ext}) = \frac{i(t)}{\frac{d}{dt}v_{ext}(t)}. \tag{3.3}$$

The external current is simply the ratio of the voltage across the sense resistor to it's resistance,

$$i(t) = \frac{v_s(t)}{R_s}. \tag{3.4}$$

The total capacitance is calculated for the rising edge of the voltage pulse. Fig. (3.5) shows the ideal C-V curve of an ACTFEL device. Again, below threshold the ideal curve shows the total capacitance of the capacitor stack while above threshold the insulator capacitance value is found.

4. EXPERIMENTAL ASSESSMENT OF THE IMPACT EXCITATION EFFICIENCY

In this chapter, the investigated ACTFEL devices and the experimental procedure for measuring the impact excitation efficiency are described. Signal processing issues and error considerations are also discussed. Experimental results and a discussion of these results are presented in Chapter 5.

4.1. Description of the Investigated Devices

Two devices are investigated in this work. Both devices are fabricated by Planar America in Beaverton, Oregon. The two ACTFEL devices studied are a ZnS:Mn device fabricated by coevaporation of ZnS and Mn and a $CaSrGa_2S_4$: Ce fabricated by sputtering a mixed solid source. The ZnS:Mn ACTFEL device is chosen because its electrical characteristics are almost ideal, with no measurable dynamic space charge generation, so it is expected to perform well with the field-control circuit. The ZnS:Mn ACTFEL device is also the industry standard, making its performance technologically relevant. Finally, almost all high-field transport Monte Carlo simulations have focussed on ZnS:Mn; thus, the impact excitation efficiency measurements performed within the context of this thesis will be useful for the "tuning" of unknown parameters in the Monte Carlo simulation. The $CaSrGa_2S_4$: Ce ACTFEL device is chosen because it is one of the most advanced blue devices yet to be developed. Thus, its performance is also of technological significance. Additionally, previous research [25] indicates that there is a negligible amount of dynamic space

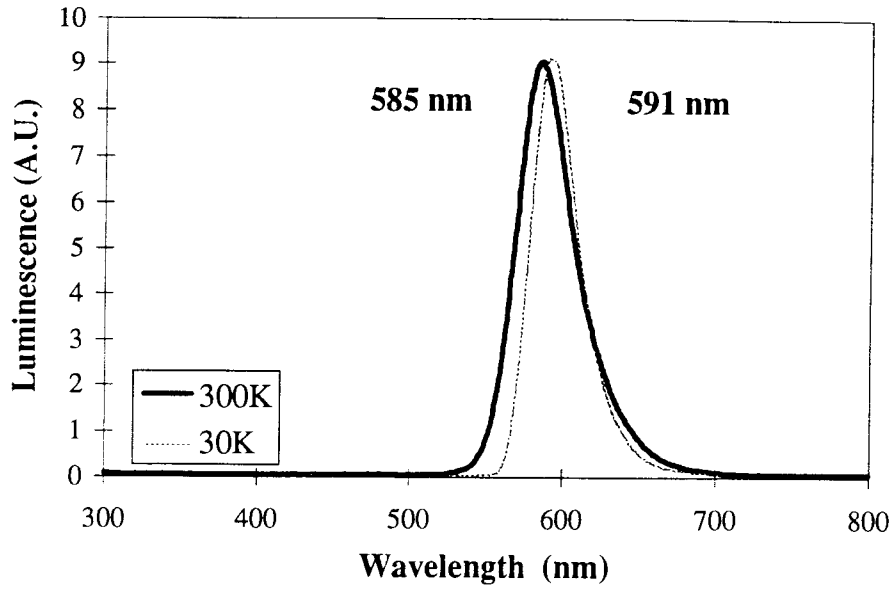

FIGURE 4.1. Emission spectrum for a ZnS:Mn ACTFEL device.

charge generation in the $CaSrGa_2S_4$: Ce ACTFEL device, so that the field-control circuit is expected to work well with it also.

The evaporated ZnS:Mn ACTFEL device emits a broad emission centered at 585 nm at room temperature and shifted to 591 nm at 30 K, as shown in Fig. 4.1. Unfortunately, no information was available regarding the phosphor thickness or the insulator thicknesses of this device. However, it is known that the measured C-V capacitance values for ZnS:Mn ACTFEL devices usually correspond well to the capacitance values calculated from the layer thicknesses and the dielectric constants. The measured C-V phosphor and insulator capacitances are $18 \pm 1\,\mathrm{nF/cm^2}$ and $21 \pm 1\,\mathrm{nF/cm^2}$, respectively. This leads to an estimate of the phosphor thickness of 387 ± 20 nm, assuming a phosphor relative dielectrical constant of 8.

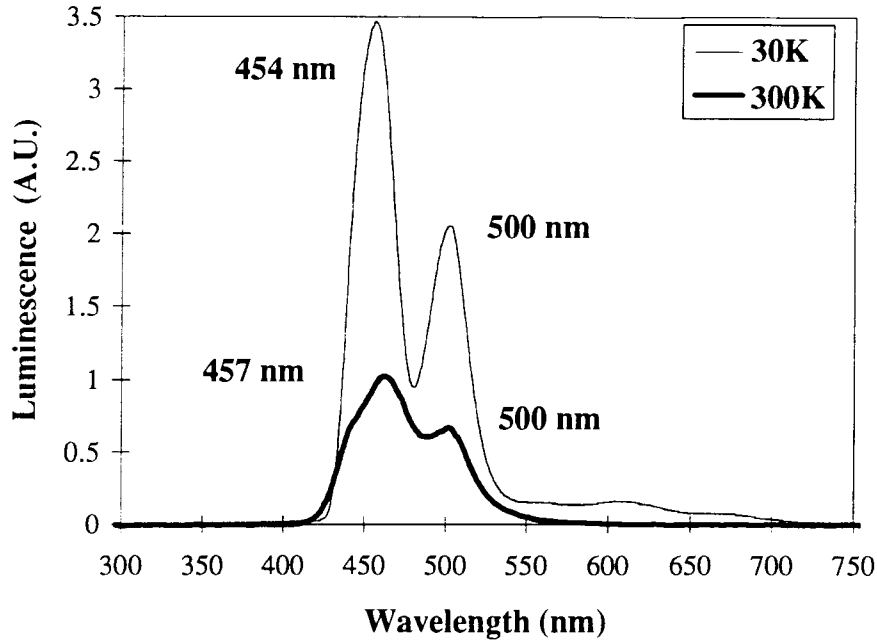

FIGURE 4.2. Emission spectrum for a $CaSrGa_2S_4$: Ce ACTFEL device.

The $CaSrGa_2S_4$: Ce ACTFEL device shows two emission peaks, Fig. 4.2, one centered at 454 nm and one centered at 500 nm. This device has two different insulator layers. The top layer is barium-tantalate (BTO) with a thickness of 300 nm and a relative dielectric constant of 18. The bottom layer is aluminum-titanium oxide (ATO) with a thickness of 260 nm and a relative dielectric constant of 25. The phosphor layer thickness is 435 nm and the dielectric constant is 15. The calculated insulator capacitance value for this structure is 33 nF/cm^2. The experimentally measured value for the insulator capacitance at room temperature is 30 ± 1 nF/cm^2 and at 30 K is 26 ± 1 nF/cm^2.

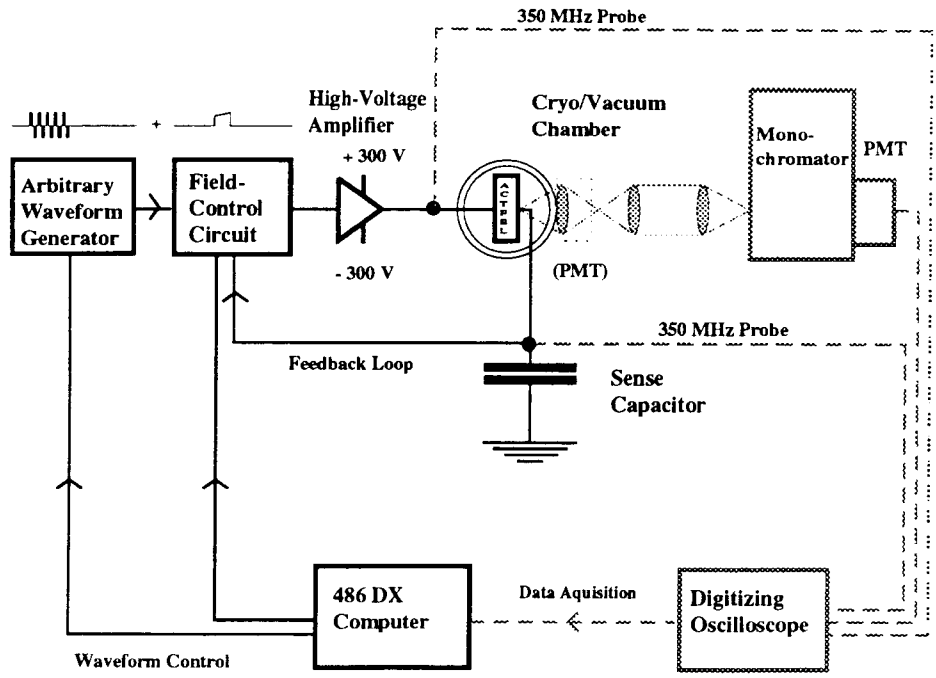

FIGURE 4.3. Experimental setup.

4.2. Experimental Setup for the Impact Excitation Efficiency Measurement

The experimental setup for the impact excitation efficiency measurement is shown in Fig. 4.3 and consists of the ACTFEL device, a closed-cycle helium refrigeration system, a bipolar high-voltage amplifier, a Wavetek model 395 arbitrary waveform generator, and the field-control circuit. A Chromex 500SM scanning monochromator is used for spectrally-resolved measurements. A Hamamatsu R928 photomultiplier tube (PMT) biased at 270-900 V is used for optical detection. A Tektronix TDS 420 four channel digitizing oscilloscope and two Tektronix P61 138 probes are used for data monitoring. The experiment is controlled by a 486 DX Personal Computer through a GBIB data bus.

The experimental setup is operated in the following way. The device is mounted on a copper cold stage in the vacuum chamber of the cryostat. The driving waveform is generated by the arbitrary waveform generator and the field-control circuit. The driving waveform is amplified by the high-voltage amplifier before it is applied to the ACTFEL device. The computer is used to control the amplitude of the waveform, as well as the repetition rate of the signal. The applied voltage and the response signal are monitored via the oscilloscope. The applied voltage is probed across the ACTFEL device and any charge transfer in the phosphor is monitored by recording the voltage across the sense capacitor which is connected in series with the ACTFEL device. The optical response of the device is detected and amplified by the photomultiplier. In the case of spectrally-unresolved measurements, the photomultiplier is mounted directly onto the vacuum chamber of the cryostat. For spectrally-resolved measurements, the monochromator is inserted between the cryostat and the photomultiplier. All three signals: the applied voltage, the sense capacitor voltage, and the photomultiplier current are monitored by the oscilloscope and downloaded to the computer for further data processing.

4.3. Driving Waveform

The complex driving waveform used for the impact excitation experiment, Fig. 4.4, requires a more detailed explanation. The driving waveform consists of three distinct parts: a prepulse sequence, a dead period, and a field-control pulse. The prepulse sequence consists of 40 rectangular bipolar voltage pulses at a frequency of 10 kHz. The purpose of the prepulse sequence is to source electrons from interface states and to transfer them back and forth in the phosphor layer until a steady-state distribution is reached in which interface states at one interface are

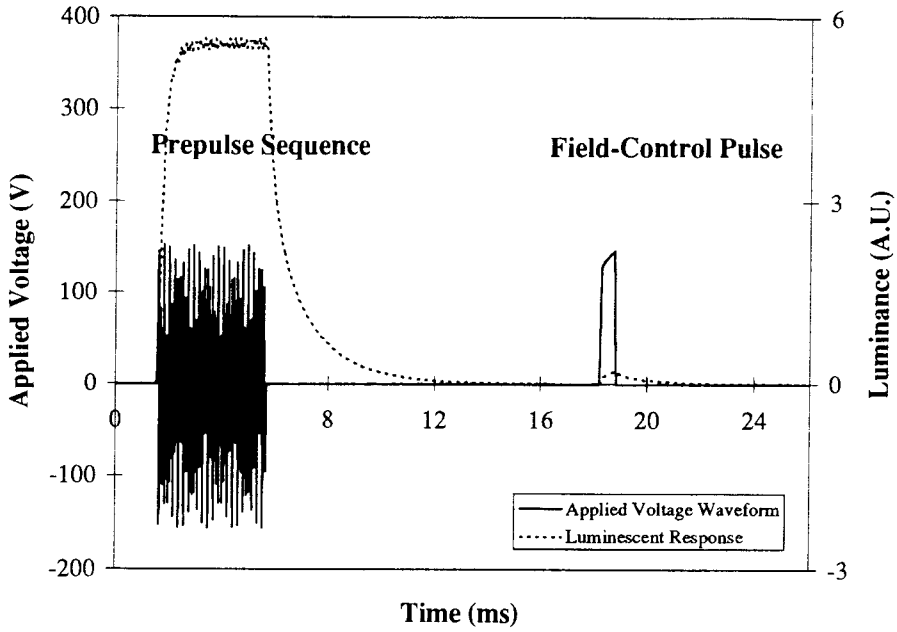

FIGURE 4.4. The driving waveform for the impact excitation efficiency measurement and the transient luminescent response.

filled to a level typical of ACTFEL operation. The prepulse sequence ends with a pulse of negative polarity. After a dead time, during which the luminescence signal (due to the prepulses) decays, the field-control pulse is applied. The field-control pulse is of positive polarity. That is, the field-control pulse is of opposite polarity to the last pulse of the prepulse sequence so that charge is sourced from the interface in which the interface states are filled. The shape of the field-control pulse is determined by the charge transfer in the ACTFEL device and the negative feedback through the field-control circuit. The duration of the field-control pulse is adjustable. The calibration of the field-control circuit is explained in Section 4.4. The impact excitation efficiency is calculated from the charge transfer during the field-control pulse and the corresponding luminescence, as discussed in Section 4.6.

4.4. The Field-Control Circuit

There are many applications in which it is desired to keep the phosphor field constant. This may be accomplished using a control circuit, henceforth referred to as a "field-control circuit".

In this application a field-controlled pulse is added to the standard ACTFEL waveform obtained from an arbitrary waveform generator. The arbitrary waveform generator produces a sequence of high frequency bipolar rectangular voltage pulses. This waveform sequence is referred to as prepulses. During the dead time between prepulse groups, the field-control pulse is inserted. The process of inserting and timing the field-control pulse is schematically represented by a "switch" in the diagram of the electrical setup in Fig. 4.5. The resistances R3 and R7 are used to ensure that both signals, the field control pulse and the prepulses, have the same impedance. The essential part of the circuit is the differential amplifier which can lock the phosphor field, by means of negative feedback, to a constant value controlled by the variable supply voltage V_1. To achieve this goal, the differential amplifier needs to be calibrated for each ACTFEL sample. To be more specific, it needs to be calibrated for each value of insulator capacitance.

4.4.1. Calibration Equation for the Field-Control Circuit

In this subsection, the possibility of maintaining a constant phosphor field by means of a field-control circuit is investigated. Analysis of the dynamic phosphor field equation leads to a calibration equation by which the appropriate gain of the differential amplifier may be determined. The phosphor field after the breakdown of the phosphor capacitance is given by

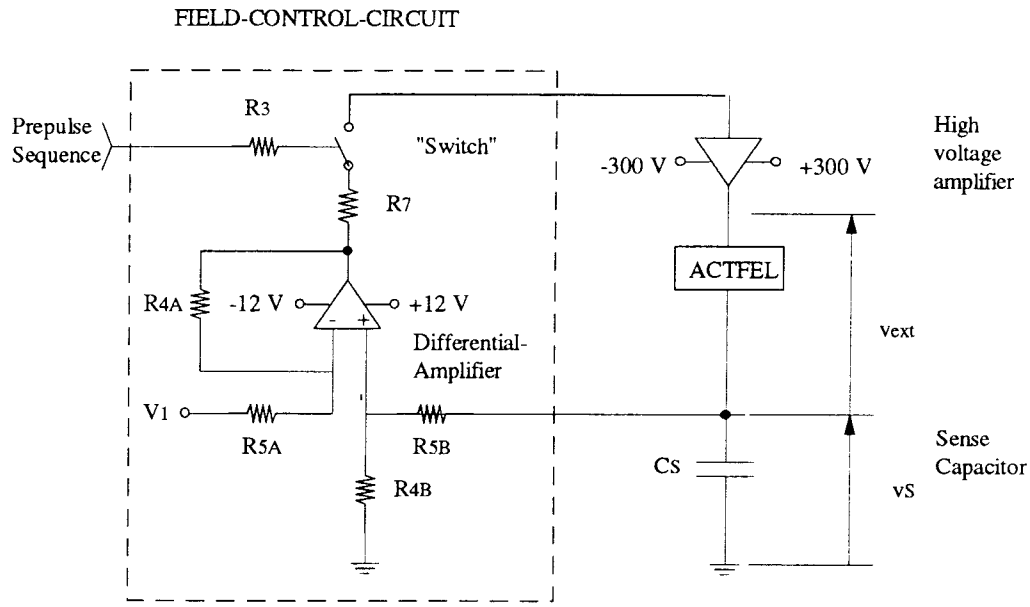

FIGURE 4.5. A schematic of the field-control circuit after the breakdown of the phosphor capacitance.

$$f_p = -\frac{1}{d_p}\left(v_{ext} - \frac{1}{C_i}Q_{ext}\right). \tag{4.1}$$

As described in Subsection 2.2.2, the time behavior of the phosphor field in an ACTFEL device is described by a dynamic phosphor field equation with respect to externally measurable parameters,

$$\frac{df_p}{dt} = -\frac{1}{d_p}\left(\frac{dv_{ext}(t)}{dt} - \frac{C_s}{C_i}\frac{dv_s(t)}{dt}\right). \tag{4.2}$$

This equation suggests that the phosphor field may be clamped to a constant value if the slew rate of the externally applied voltage v_{ext} equals the induced voltage change at the sense capacitor so that $\frac{d}{dt}f_p = 0$. This last requirement is achieved, according to Eqn. (4.2), by ensuring that:

$$\frac{dv_{ext}(t)}{dt} = \frac{C_s}{C_i}\frac{dv_s(t)}{dt}. \tag{4.3}$$

This kind of field-clamping is sometimes observed in ACTFEL devices during the rising edge of a standard applied rectangular waveforms. Maintaining a constant phosphor field by means of standard rectangular waveforms is not practical, however, since the magnitude of the phosphor field cannot be controlled to any practical degree by this approach. The field-control circuit, described below, offers a more practical way of actively controlling the phosphor field.

A schematic for the circuit used to control the phosphor field is shown in Fig. 4.5. The phosphor field amplitude is set by the voltage, V_1 applied to one input of the differential amplifier which is the heart of the field-control circuit. The other input to the differential amplifier is the voltage from the sense capacitor. The feedback signal arising from the output of the differential amplifier, which is then sent to the high voltage amplifier, is determined by the difference of V_1 and the sense capacitor voltage. Thus, the external voltage applied to the ACTFEL device is given by

$$v_{ext}(t) = G_{Cir}\frac{R_4}{R_5}(v_s(t) - V_1). \tag{4.4}$$

The total gain of the feedback loop is comprised of the gain of the differential amplifier, $\frac{R_4}{R_5}$, and the gain of the remaining circuit, G_{Cir}, which includes the high voltage amplifier. Substituting Eqn. (4.4) into Eqn. (4.1) and rearranging yields

$$f_p(t) = -\frac{1}{d_p}\left[\underbrace{\left(G_{Cir}\frac{R_4}{R_5} - \frac{C_s}{C_i}\right)v_s(t)}_{time\ dependent} - \underbrace{G_{Cir}\frac{R_4}{R_5}V_1}_{time\ independent}\right]. \tag{4.5}$$

The validity of this equation requires that the feedback loop react instantaneously to any change in the charge transfer. This is not the actual case but the time constant of the feedback circuit is assumed to be sufficiently short that this assumption is valid in the field-control regime.

It is seen in Eqn. (4.5), that if the phosphor field is to be kept constant, the first term in the square brackets, which is the only time-dependent term, has to be equated to zero; setting the quantity in the parentheses to zero results in a specification of the calibration equation:

$$\frac{R_4}{R_5} = \frac{C_s}{C_i}\frac{1}{G_{Circ}}. \tag{4.6}$$

When Eqn. (4.6) applies, the phosphor field is constant at a value given by:

$$f_p = \frac{1}{d_p} G_{Cir} \frac{R_4}{R_5} V_1. \tag{4.7}$$

Note that once the ACTFEL device is chosen and the control-circuit is calibrated according to Eqn. (4.6), all of the terms in Eqn. (4.7) are constants. Thus Eqn. (4.7) confirms that V_1 controls the phosphor field, f_p.

Again it should be pointed out that the validity of Eqn. (4.7) depends on the assumption that the time constant of the feedback loop of the complete circuit, shown in Fig. 4.5 is much smaller than the duration of the field-control pulse. The upper frequency limit of the high voltage amplifier is about 10 kHz. The differential amplifier shows a corner frequency of 3 kHz, its amplification is reduced to about 50% of its maximum value for a signal frequency of 10 kHz. Thus, the frequency limit is expected to be around 10 kHz. The measured charge transients show oscillations of about 0.1 ms periodicity which is consistent with the frequency limitation of the amplifier setup. The time constant is about $\frac{1}{10}$ or $\frac{1}{6}$ respectively of the used field-control pulse duration, Section 4.8.

4.4.2. Sensitivity of the Phosphor Field to the Insulator Capacitance

The primary concern of this section is how the uncertainty in the insulator capacitance determines the precision to which the phosphor field is controlled.

Assume that the calibration equation is not precisely fulfilled, due to either error in the estimation of the insulator capacitance or to inaccurate matching of the resistors, R_4 and R_5. If the calibration error arises from an uncertainty in the insulator capacitance, ΔC_i, the actual calibration equation is modified to be

$$\frac{R_4}{R_5} = \frac{C_s}{C_i + \Delta C_i} \frac{1}{G_{Cir}}. \tag{4.8}$$

If the precise value for C_i is known, the phosphor field can be calculated and found to be time-dependent. Substitution of Eqn. (4.8) into Eqn. (4.5) and rearranging leads to

$$f_p = \frac{1}{d_p} \frac{C_s}{C_i + \Delta C_i} \left[\underbrace{\frac{\Delta C_i}{C_i} v_s(t)}_{time\ dependent} + V_1 \right]. \tag{4.9}$$

Equation (4.9) shows that maintaining a constant phosphor field depends critically on the precision to which C_i is known. Any error in the insulator capacitance results in a deviation in the phosphor field from a constant value which is manifest as the time-dependent term in the bracket of Eqn. (4.9).

Now assume that the C_i value is not accurately known. In this case, the field-control circuit is calibrated using an erroneous value for the insulator capacitance. The calibration equation becomes again Eqn. (4.8). Substituting Eqn. (4.8) into Eqn. (4.5) and recognizing that C_i in Eqn. (4.5) should be replaced by $C_i + \Delta C_i$ yields

$$f_p = \frac{1}{d_p} \frac{C_s}{C_i + \Delta C_i} V_1. \tag{4.10}$$

Thus, Eqn. (4.10) indicates that using an erroneous insulator capacitance in the calibration equation and in the phosphor field equation leads to a time-independent, but erroneous estimate of the phosphor field. It should be stressed that it is always possible to obtain a constant phosphor field if the value of the insulator capacitance used in the calculation for the phosphor field corresponds precisely to the value for which the field-control circuit is calibrated. However, the actual phosphor field will only be constant when C_i is equal to the actual insulator capacitance. Thus, it is crucially important to determine the insulator capacitance as accurately as possible.

4.4.3. Experimental Calibration of the Field-Control Circuit

The experimental calibration of the field-control circuit is accomplished as follows. The insulator capacitance is assessed from Q-V and C-V plots as described in Section 3. For the generation of these plots a bipolar trapezoidal voltage pulse is applied to the device. The c_i and c_t values (capacitance per unit area) are taken from the slope of a straight line fit to the Q-V curve. The uncertainty in c_i is estimated from the oscillations in the C-V curves. These oscillations are attributed to the digital nature of the waveforms generated by the arbitrary waveform generator. Q-V and C-V curves for the ZnS:Mn ACTFEL device are shown in Figs. 4.6 and 4.7 to illustrate this procedure. The effective capacitance values found for the devices used are listed in Table (4.1). The c_t value is adjusted within the uncertainty estimated from the C-V curves, such that the continuity of the internal charge transient is given, Fig. 4.8, [5]. An incorrect value for the total capacitance results in discontinuities in the internal charge transients. This way, the uncertainty in c_t can be reduced.

	ZnS:Mn		$CaSrGa_2S_4$: Ce	
	300 K	40 K	300 K	40 K
c_t $(\frac{nF}{cm^2})$	9.7 ± 0.1	9.5 ± 0.1	12.6 ± 0.1	12.1 ± 0.1
c_i $(\frac{nF}{cm^2})$	21 ± 1	21 ± 1	30 ± 1	26 ± 1
c_p $(\frac{nF}{cm^2})$	18 ± 1	17 ± 1	22 ± 1	23 ± 1

TABLE 4.1. Experimentally determined capacitance values for ZnS:Mn and $CaSrGa_2S_4$: Ce ACTFEL devices.

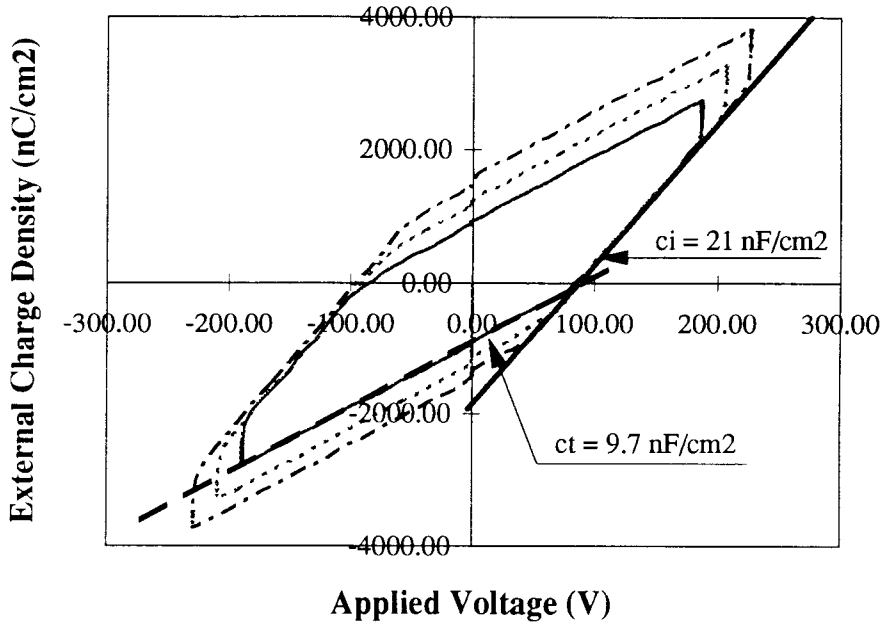

FIGURE 4.6. Q-V curve for a ZnS:Mn ACTFEL device at 300 K.

The circuit gain is determined by measuring the output of the differential amplifier with respect to the applied voltage. The ratio of the resistances, R_4 and R_5, calculated from Eqn. (4.6) can be obtained using resistance values of various orders. However, the magnitude of the resistances employed requires some consideration. The magnitude of the resistances used is bound by two constraints: the input impedance of the differential amplifier and the discharge of the sense capacitor. Current will flow through the amplifier if the resistances are of the order of the input resistance of the differential amplifier. The input resistance of the differential amplifier is 45 MΩ. If the resistances are small, the voltage on the sense capacitor decays quickly. The RC time constant of the calibration resistors and the sense capacitor needs to be larger than the pulse width of the field-control pulse. Resistances of the order of several hundred kilo-ohms yield an RC time constant for the discharge of the sense capacitor which is about a hundred times the duration of the field control pulse. That is, the sense capacitor holds about 99% of its initial charge over a pulse duration of 1 ms. Thus, resistances in the range of kilo-ohms are used in these experiments.

4.5. Optical Signal Calibration

The luminescence signal emitted from the ACTFEL device has to pass through several optical interfaces before it reaches the photomultiplier tube. Regardless of whether the optical signal is spectrally resolved or unresolved, it has to pass through the infrared filter of the heat shield in the vacuum chamber as well as through the quartz glass window of the shroud. The optical signal is then detected by the photomultiplier and monitored by the oscilloscope. The infrared filter of the heat shield has the purpose of shielding the device from incident thermal radiation

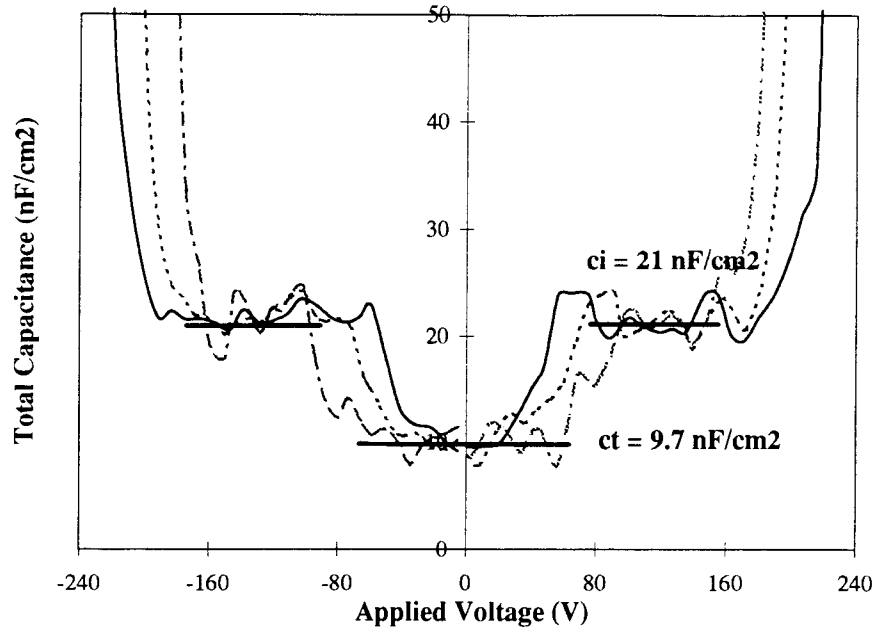

FIGURE 4.7. C-V curve for a ZnS:Mn ACTFEL device at 300 K.

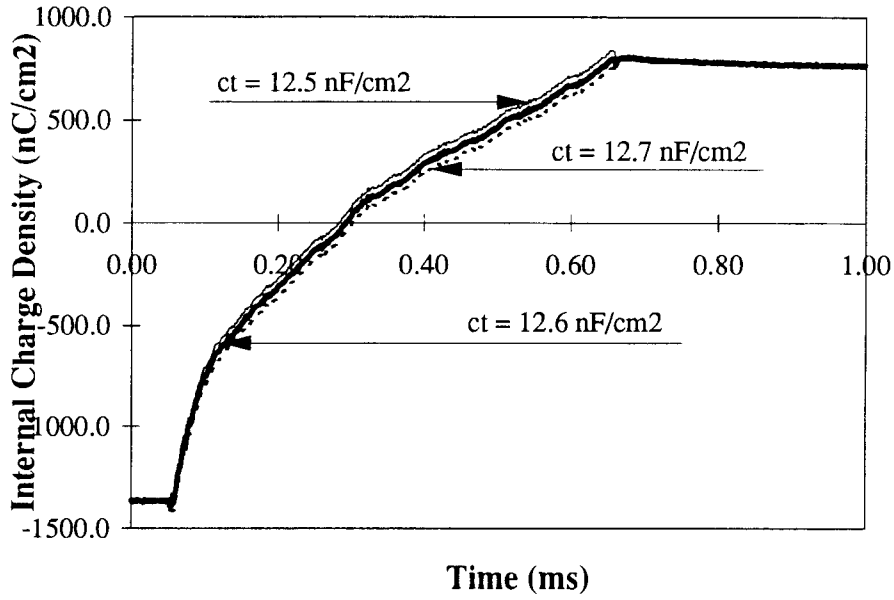

FIGURE 4.8. Estimation of the total capacitance from the continuity of the internal charge curves of a $CaSrGa_2S_4$:Ce ACTFEL Device.

and to allow for transmission in the visible region. The infrared filter is fabricated from Schott KG1 glass which transmits at least 80% of the visible light between 350 nm and 640 nm. The transmittance curve of the KG1 glass shows oscillations around a transmission efficiency of 90% in a range of 360-590 nm. These oscillations are small, $\sim$ 3%. No correction has been made to account for the transmittance curve of the infrared filter. The observation window of the shroud is made of quartz glass; its variation in transmittance is negligible over the visible spectrum.

The strong wavelength and power supply voltage dependent sensitivity of the photomultiplier is accounted for in the intensity calculations. The radiant sensitivity values of the photocathode are taken from the sensitivity curve supplied by Hamamatsu with the PMT. Radiant sensitivity corrections are made in 25 nm steps over a range from 400 to 700 nm. The sensitivity value closest to the operating wavelength is chosen for the signal calibration. The current amplification of the photomultiplier is dependent on the supply voltage as follows [24],

$$G = KV_{supp}^{m}. \tag{4.11}$$

The current amplification depends as a power law on the supply voltage. The amplification exponent, m, is determined from a comparison of the current gain values of two different supply voltages for the same incident signal. A value of 6.085 is found for m. The proportionality constant, K, is taken from the specifications in the photomultiplier manual. The proportionality factor is independent of the supply voltage and the wavelength of the incident radiation. Since the final results are only qualitative, the actual value of K is not important for this impact excitation efficiency measurement.

The photomultiplier current, I_L, depends on the incident photon flux, Φ_e, the radiant sensitivity of the photomultiplier cathode, $S(\lambda)$, and the current gain of the photomultiplier. Thus, the current output of the photomultiplier is given by

$$I_L = K V_{Supp}^m S(\lambda)_{rad} \Phi_e. \tag{4.12}$$

The photomultiplier current is monitored as a voltage across the oscilloscope input resistance. The input resistance is chosen such that the response time of the oscilloscope is smaller than the characteristic time of the incoming signal. Experimentally it is found that an input resistance of $2\,\mathrm{k}\Omega$ is appropriate .

The incident flux is assessed via the following equation

$$\Phi_e = \frac{1}{K V_{Supp}^m S(\lambda)_{rad} R_L} V_L. \tag{4.13}$$

By means of this equation, signals obtained using different photomultiplier amplifications, wavelengths, or input resistances can be compared, as long as the experimental setup is not changed.

In the particular case of spectrally-resolved measurements, the monochromator efficiency needs to be considered as well. The lenses needed for guiding the signal into the monochromator are assumed to show no wavelength dependence for transmission in the visible spectrum. It is also assumed that the reflectance of the mirrors in the monochromator is the same for all wavelengths in the visible range. Thus, the efficiency of the monochromator is mainly dependent on the grating efficiency. Two gratings are available: one with a 500 nm blaze and one with a 1.2 μm blaze. For the best efficiency in the visible range, the 500 nm blaze is most effective. In order to compare the luminescence at two different wavelengths, the relative efficiency of the monochromator grating needs to be taken into account.

Due to the single broad emission line of the ZnS:Mn ACTFEL device, the excitation efficiency measurement for this device is performed spectrally unresolved.

In this case the photomultiplier is mounted directly onto the window of the vacuum chamber.

The $CaSrGa_2S_4$: Ce ACTFEL device shows two emission lines and, hence, the measurement of the excitation efficiency is conducted spectrally-resolved by means of the monochromator. Since the calculated and the measured capacitance values for this device do not correspond, the experiment is performed twice; once for each capacitance value. For the experimental assessment of the excitation efficiency by means of the measured insulator capacitance, the grating with a 500 nm blaze was used. However, because of an oversight, the 1.2 μm blaze was used for the experiments on the $CaSrGa_2S_4$: Ce which were performed calibrating the field-control circuit with the theoretically expected value for the insulator capacitance. In this case, the monochromator was operated at low efficiency. The low efficiency was compensated by a higher amplification of the photomultiplier.

4.6. Calculation of the Impact Excitation Efficiency

The applied voltage, the voltage across the sense capacitor, and the photomultiplier signal voltage are downloaded to a PC by means of a Visual Basic program and saved as an ASCII data file. The data files names are coded with respect to the external parameters of the experiment such that an EXCEL macro can automatically access the relevant data for the required data processing and graphical display. The EXCEL macro calculates the internal charge and phosphor field transients and evaluates the conduction charge, polarization charge, integrated luminescence, and the impact excitation efficiency.

The impact excitation efficiency is evaluated from the field-control pulse portion of the waveform. The conduction charge is evaluated from the internal charge

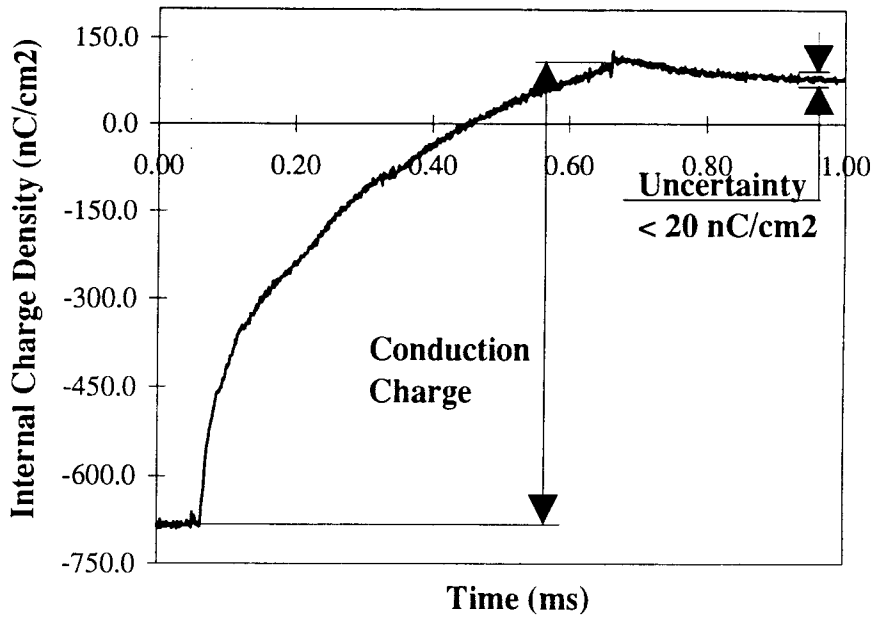

FIGURE 4.9. Assessment of the conduction charge.

transient curve as the difference between the maximum charge and the initial polarization charge due to the last prepulse, as shown in Fig. 4.9. The internal charge transient curve is rather noisy. Thus, the maximum charge is estimated as the average charge over 20 μs of the signal just after the end of the field-control pulse, Fig. 4.9. The luminescent response is the integral over the whole luminous signal due to the field-control pulse. The integration length of the luminescent response integral begins at the onset of the field-control pulse and ends with the termination of the luminescent transient signal, which occurs well after the field-control pulse has ended. The impact excitation efficiency is then the ratio of the luminescent response, L = $\int$ l(t)dt, and the conduction charge.

$$\eta_i = \frac{L}{q_{cond}} \tag{4.14}$$

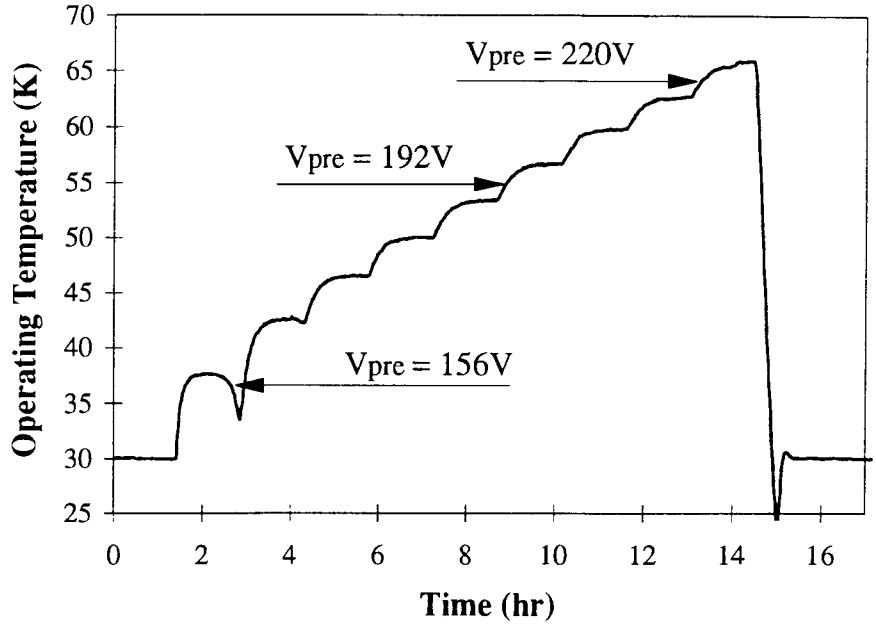

FIGURE 4.10. Heating at low temperature during device operation for a ZnS:Mn ACTFEL device.

In order to reduce statistical uncertainties, a set of excitation efficiencies versus phosphor field curves are taken for various prepulse voltages. The excitation efficiency is taken to be the weighted average of these sets of excitation efficiencies,

$$\eta = \frac{\sum_{i=1}^{n} \frac{1}{\Delta\eta_i}\eta_i}{\sum_{i=1}^{n} \frac{1}{\Delta\eta_i}} \tag{4.15}$$

where $\Delta\eta_i$ is the uncertainty of the excitation efficiency of one data set. The uncertainty calculation is explained in the next section.

4.7. Uncertainty Calculations for the Impact Excitation Efficiency

Uncertainties of the impact excitation efficiency with respect to the device temperature, the phosphor field, the luminescence, and the conduction charge are considered in this section. It is found that during low temperature operation, the

temperature increased as soon as conduction in the phosphor began, as shown in Fig. 4.10. This temperature rise is attributed to power dissipation in the ACTFEL device. Since the device temperature increases with every increment of the prepulse voltage amplitude, it is concluded that the cryostat's cooling rate is no longer sufficient to accomodate the power dissipation concomitant with the current. Therefore, the prepulse voltage is varied over only a narrow voltage range in order to maintain a fairly constant temperature and to avoid temperature-related uncertainties in the determination of the excitation efficiency.

At low temperature, the impact excitation efficiency for the ZnS:Mn ACTFEL device is calculated for a set of only three prepulse voltages (178 V, 185 V, 192 V) due to the variation of the device temperature. Thus the mean operating temperature is 52 K for this measurement. The excitation efficiency for the $CaSrGa_2S_4$: Ce ACTFEL device is obtained using prepulse voltages of 185, 188, and 192 V; the mean temperature is 40 K.

Uncertainties in the impact excitation efficiency originate from uncertainties in the magnitude of the conduction charge and the luminescent response. The conduction charge uncertainty is due to noise in the charge transient curve which is estimated as 10 nF/cm^2, in Fig. 4.9. Since the conduction charge is measured as a difference in the internal charge transient curve, the total uncertainty in the conduction charge is 20 nF/cm^2.

The noise in the integrated luminescent response is estimated from an integration of the dark current of the PMT over an equally long period as the luminescent response.

From the uncertainties in the conduction charge and the luminescent response, the uncertainty in the excitation efficiency for a single prepulse amplitude is calculated using the following formula,

$$\Delta\eta_i = \eta_i \sqrt{\left(\frac{\Delta L}{L}\right)^2 + \left(\frac{\Delta q}{q}\right)^2}. \tag{4.16}$$

The final excitation efficiency is the weighted average of the excitation efficiencies found for a set of prepulse amplitudes, as described in Section 4.6. The uncertainty of this averaged efficiency is calculated as a weighted root mean square deviation

$$\Delta\eta = \sqrt{\frac{\sum_{i=1}^{n} \frac{1}{\Delta\eta_i}(\eta_i - \eta)^2}{(n-1)\sum_{i=1}^{n} \frac{1}{\Delta\eta_i}}}. \tag{4.17}$$

The uncertainty in the impact excitation efficiency is determined primarily by uncertainties in the conduction charge and luminescent response in the threshold regime where the signal-to-noise ratio is small.

The last uncertainty considered is due to the phosphor field. Taking the voltage errors to be negligibly small, assuming that the oscilloscope is well calibrated, then the only important uncertainties in the phosphor field equation are the insulator capacitance and the phosphor thickness. Hence, an error analysis with respect to the insulator capacitance and the phosphor thickness leads to

$$df_p = \sqrt{\left(\frac{\partial f_p}{\partial C_i}\right)^2 dC_i^2 + \left(\frac{\partial f_p}{\partial d_p}\right)^2 dd_p^2}. \tag{4.18}$$

The partial derivative of the phosphor field with respect to the insulator capacitance may be evaluated by taking the partial derivative of Eqn. (4.1)

$$\frac{\partial f_p}{\partial C_i} = \frac{-Q_{ext}}{d_p C_i^2}, \tag{4.19}$$

where any change in the external charge with respect to a change in the insulator capacitance is neglected.

The other uncertainty in the phosphor field calculation is the phosphor thickness. The partial derivative with respect to the phosphor thickness may be evaluated by taking the partial derivative of Eqn. (4.1)

$$\frac{\partial f_p}{\partial d_p} = f_p \frac{1}{d_p}. \tag{4.20}$$

Substituting Eqn. (4.19) and Eqn. (4.20) into Eqn. (4.18) results in

$$df_p = \frac{f_p}{d_p} \sqrt{\frac{Q_{ext}^2}{f_p^2} \frac{1}{C_i^4} dC_i^2 + dd_p^2}. \tag{4.21}$$

It can be seen from Eqn. (4.21) that, the larger the insulator capacitance, the smaller the sensitivity of the phosphor field with respect to the insulator capacitance. The accuracy of the phosphor field further depends on the amount of external charge transferred. Since the externally accumulated charge is largest towards the end of the field-control pulse, the accuracy will be worst towards the end of the pulse. The error introduced by uncertainties in the insulator capacitance is of deterministic nature and thus cannot be reduced by averaging several measurements. An upper limit for the uncertainty in the phosphor field is indicated in the results.

In summary, the temperature uncertainties of about 5 K do not seem to have a significant influence on the excitation efficiency. The signal-to-noise ratio in the conduction charge and the luminescent response near threshold limit the accuracy of the excitation efficiency in the threshold regime. The uncertainty in the phosphor field becomes larger with increasing phosphor field and increasing prepulse amplitude. Hence, while the signal-to-noise ratio at high fields is large, the uncertainty in the phosphor field becomes significant (see Fig. 5.7 later).

4.8. Determination of Operating Parameters

Before the impact excitation efficiency measurement can be accomplished, some preliminary investigations are required to determine the operating parameters and their influence on the measured impact excitation efficiency. The investigated

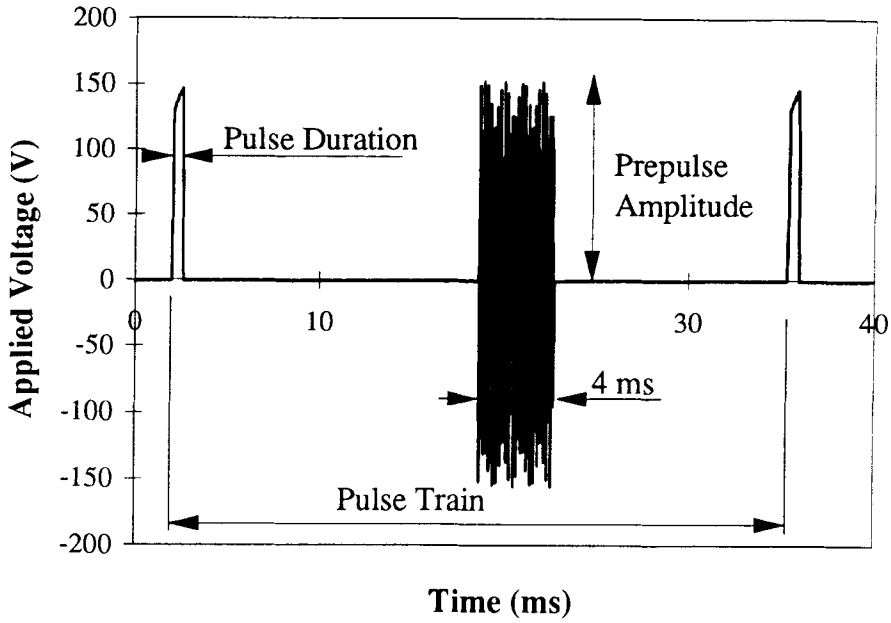

FIGURE 4.11. The investigated operating parameters: the repetition rate of the pulse train, the duration of the field-control pulse, and the amplitude of the prepulse sequence.

operating parameters are: the repetition rate of the applied waveform, the duration of the field-control pulse, and the prepulse amplitude, Fig. 4.11.

The repetition rate of the entire applied pulse train waveform and the spacing between the prepulse sequence and the field-control pulse can be varied by adjusting the frequency of the waveform generator via the control program. Measurements are obtained for a fixed field-control pulse duration of 1 ms, a prepulse voltage of 192 V, for 40 prepulses at a 10 kHz rate, a phosphor field of 2.2 MV/cm set by the field-control pulse amplitude, and a set of full pulse train widths. The results are shown in Figs. 4.12 and 4.13. For both devices, the amount of conduction charge decreases with increasing repetition rate, which also causes a shorter dead period between the prepulse sequence and the field-control pulse.

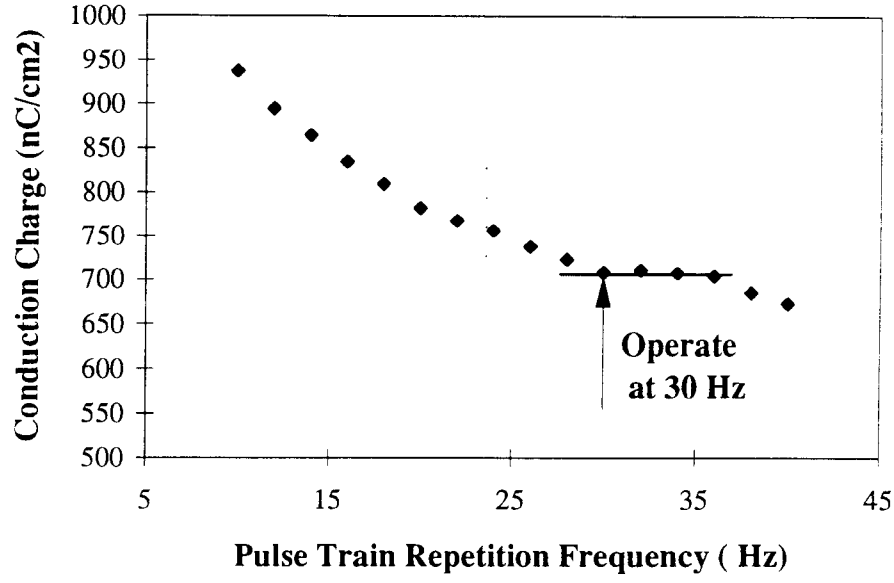

FIGURE 4.12. Influence of the pulse train repetition frequency on the conduction charge for a ZnS:Mn ACTFEL device at room temperature.

The operating frequency is chosen to occur in a range in which the conduction charge depends only weakly on the operating frequency. The operating frequencies chosen are 30 Hz for ZnS:Mn and 60 Hz for $CaSrGa_2S_4$: Ce. Those values correspond to dead times of 14.46 ms for ZnS:Mn and 4.70 ms for $CaSrGa_2S_4$: Ce. The reason for the decrease in conduction charge with increasing pulse train repetition frequency is not yet completely understood. It is assumed, that the ACTFEL element temperature increases with increasing frequency resulting in an increasing amount of electron-phonon scattering and thus less conduction charge.

Another operating parameter which needs to be defined is the duration of the field-control pulse. The behavior of the conduction charge with respect to the pulse width is monitored while the frequency and prepulse voltage are kept constant. Figs. 4.14 and 4.15 show the amount of conduction charge versus the duration of the field-control pulse. As expected, the conduction charge increases with the duration

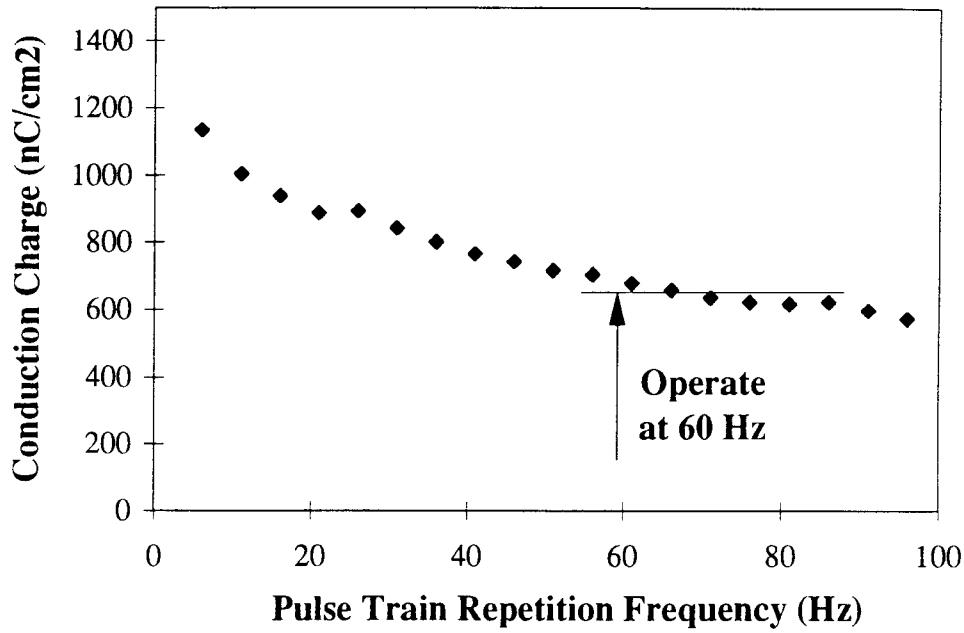

FIGURE 4.13. Influence of the pulse train repetition frequency on the conduction charge for a $CaSrGa_2S_4 : Ce$ ACTFEL device at room temperature ($V_{pre} = 192\,V$, $F_p = 2.2\,MV/cm$, $T = 1\,ms$).

of the field-control pulse. For both devices the conduction charge saturates above a certain pulse length. The operating field-control pulse lengths are chosen to be in the saturation regime. The chosen pulse durations of the field-control pulses are 1.03 ms ZnS:Mn ACTFEL device and 0.6 ms for $CaSrGa_2S_4 : Ce$ ACTFEL device.

The third operating parameter to be determined is the prepulse amplitude. In this case the repetition rate is kept constant at 30 Hz for ZnS:Mn and at 60 Hz for $CaSrGa_2S_4 : Ce$. The influence of the prepulse amplitude on the conduction charge of a ZnS:Mn ACTFEL device at roomtemperature is shown in Fig. 4.16. More conduction charge is measured for a given phosphor field, during the field-control pulse, if the prepulse amplitude is increased.

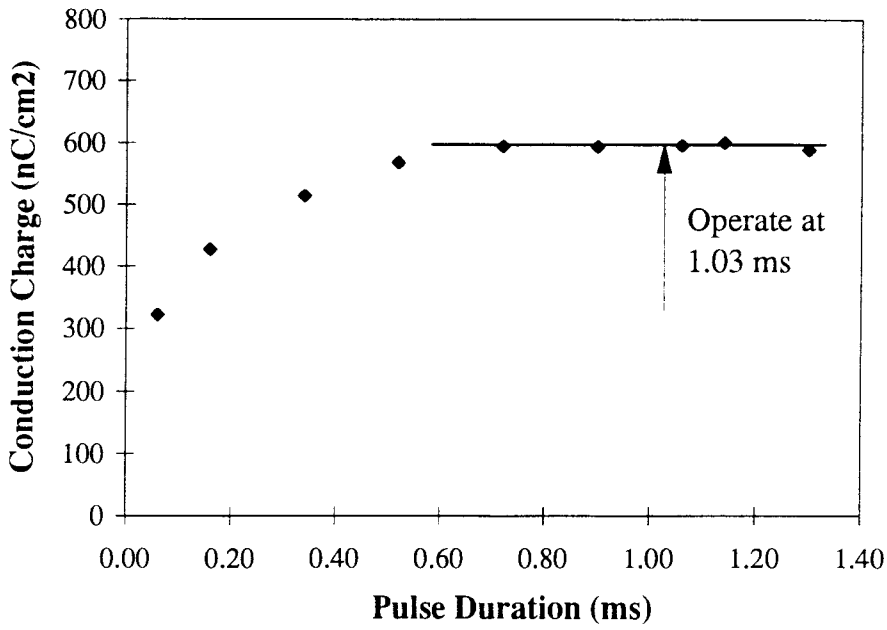

FIGURE 4.14. Influence of the pulse duration on the conduction charge for a ZnS:Mn ACTFEL device at room temperature.

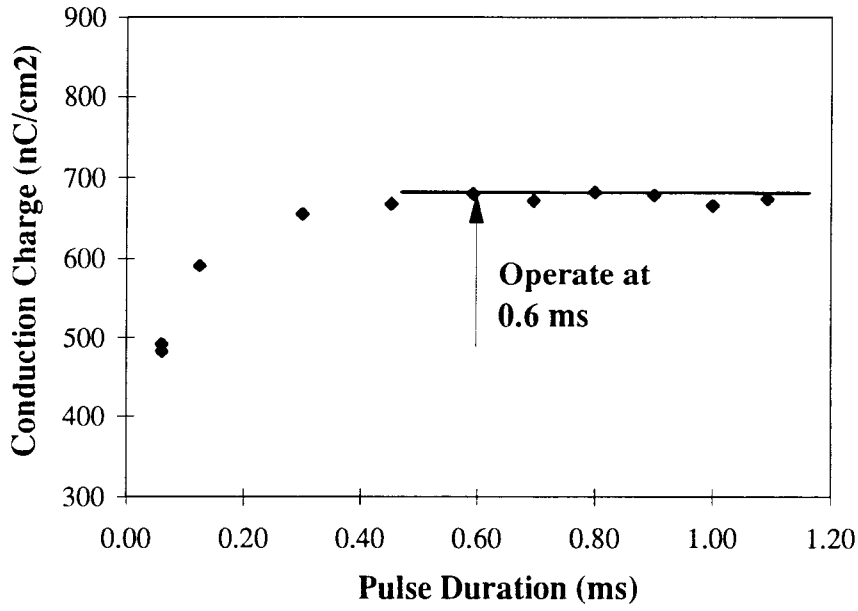

FIGURE 4.15. Influence of the pulse duration on the conduction charge for a $CaSrGa_2S_4$: Ce ACTFEL device at room temperature.

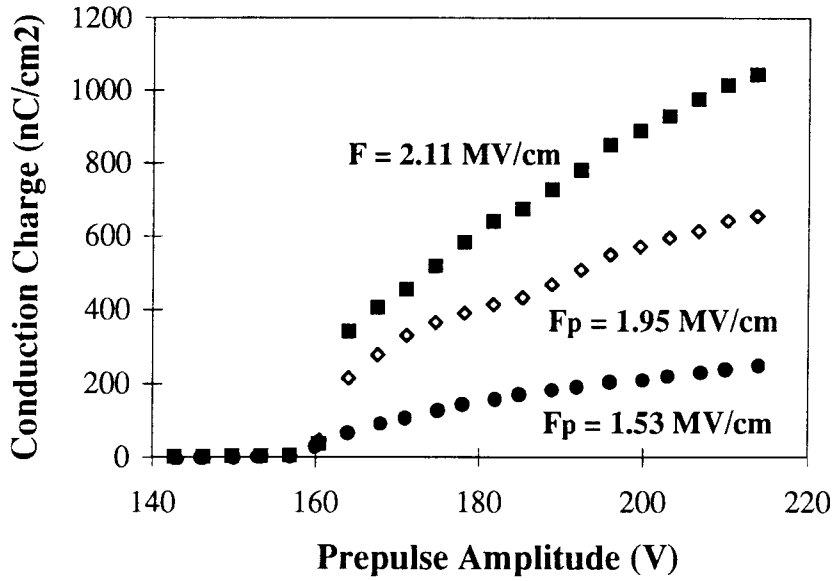

FIGURE 4.16. Conduction charge versus prepulse amplitude for fixed phosphor field for the ZnS:Mn ACTFEL device at 300 K (f = 30 Hz, T = 1.03 ms).

Figure 4.17 shows the influence of the prepulse amplitude on the excitation efficiency of a ZnS:Mn ACTFEL device at room temperature under the same conditions. The strongest change in impact excitation efficiency for a certain phosphor field occurs around and below the threshold voltage of the device. Above the threshold voltage the impact excitation efficiency does not show a strong dependence on the prepulse amplitude. The influence of the amplitude of the prepulse sequence on the measured excitation efficiency is demonstrated in Figure 4.18, which shows the impact excitation efficiencies for a ZnS:Mn ACTFEL device for three different prepulse amplitudes, around threshold voltage and 14 V above and below the threshold voltage. The impact excitation efficiency curve is shifted to much larger fields for the prepulse amplitude below threshold, while only a small shift occurs for the prepulse amplitude above threshold. The excitation efficiency behaves in a similar fashion

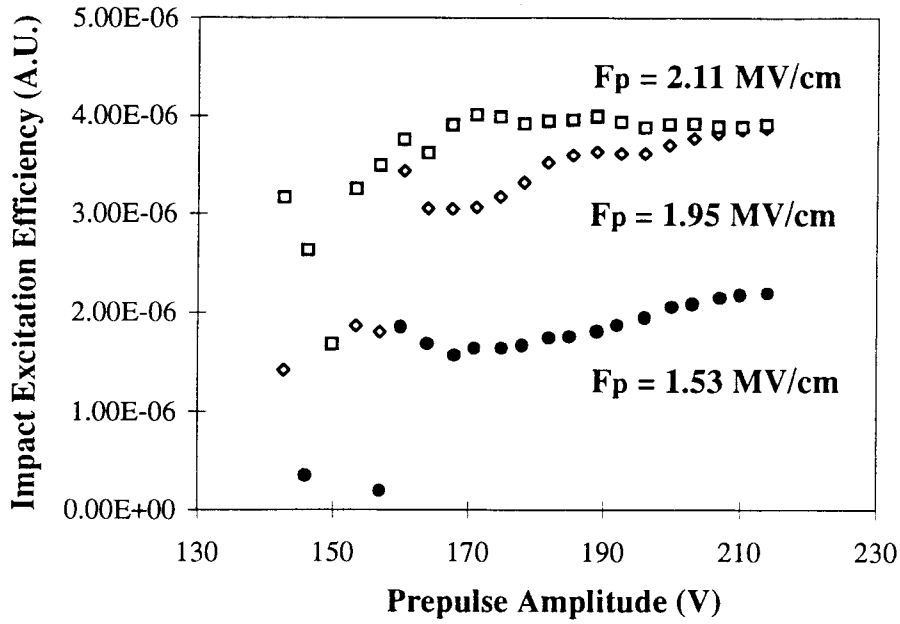

FIGURE 4.17. Excitation efficiency versus prepulse amplitude for fixed phosphor field for the ZnS:Mn ACTFEL device at 300 K (f = 30 Hz, T = 1.03 ms).

for low temperature measurements and for the $CaSrGa_2S_4$: Ce ACTFEL device. Hence, the excitation efficiency experiment is conducted by operating the device with prepulse amplitudes above the threshold voltage of the ACTFEL device.

In order to reduce the statistical uncertainy in the impact excitation efficiency experiment, measurements were conducted with several different prepulse amplitudes above the threshold voltage. The final result is then the average of the individual impact excitation efficiency curves. The prepulse amplitudes chosen for the ZnS:Mn ACTFEL device are 164, 168, 171, 175, 178 V at 300K and 178, 185, 192 V at low temperature. The prepulse amplitudes for the $CaSrGa_2S_4$: Ce ACTFEL device are 185, 188, 192 V at 300 K and at low temperature. The final results are shown and discussed in Chapter 5.

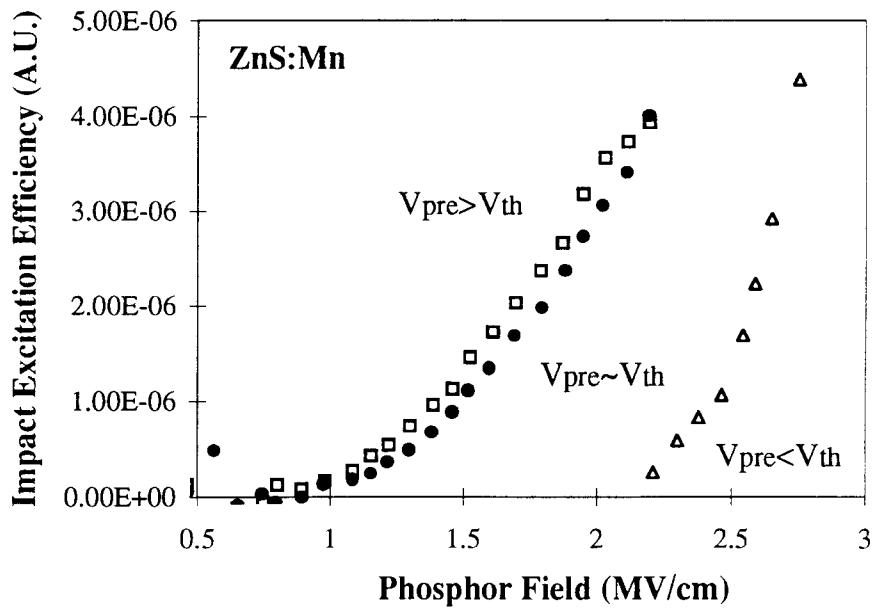

FIGURE 4.18. Excitation efficiency for prepulse amplitudes above and below the threshold voltage.

5. RESULTS & DISCUSSION

In this chapter the results of the impact excitation measurements are presented and discussed. The results for both kinds of ACTFEL devices are presented separately.

5.1. Impact Excitation Efficiency Measurement of ZnS:Mn ACTFEL devices

Figures 5.1-5.3 show the results found for the ZnS:Mn ACTFEL device. Figure 5.1 shows the conduction charge versus phosphor field for room temperature and low temperature operation. The operating parameters are: $V_{pre} = 178\,V$, $f = 30\,Hz$, $T = 1.03\,ms$. There is more conduction charge recorded for device operation at room temperature than for operation at 56 K. At room temperature, the charge transfer starts around 0.6 MV/cm, which is about 0.16 MV/cm earlier than at 56 K. The slope in the conduction charge above 1.9 MV/cm is higher for low temperature than for room temperature. The trend of the conduction charge at room temperature is extrapolated from the low temperature data to illustrate this behavior.

The reduction in conduction charge at 56 K is attributed to a reduction of phonon assisted tunneling from interface states. Thus less charge is sourced from interface states at low temperatures and low fields. The increasing slope in the conduction charge at higher fields could be due to charge multiplication in the bulk or an increasing contribution of pure tunneling emission from the interface states.

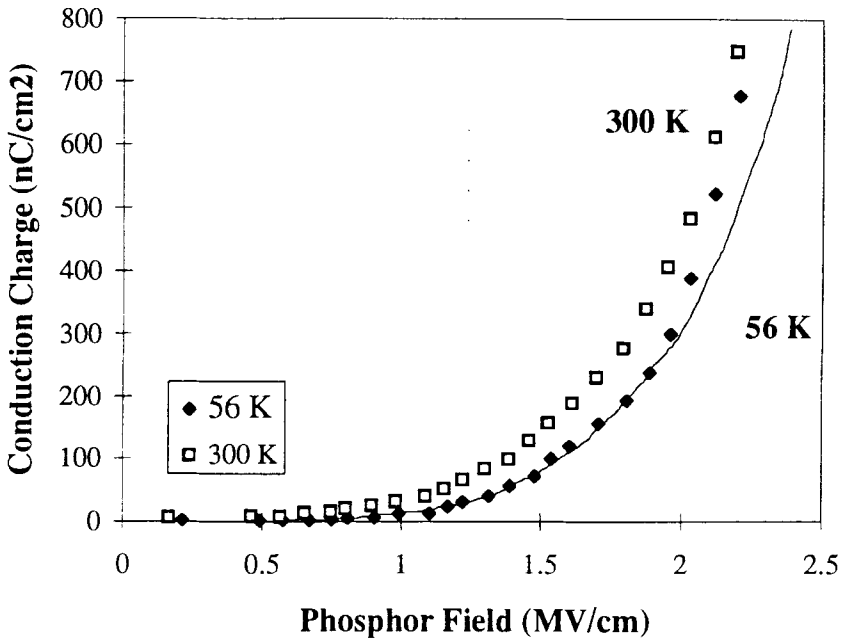

FIGURE 5.1. Conduction charge versus phosphor field for a ZnS:Mn ACTFEL device (V_{pre} = 178V).

Figure 5.2 shows the luminescence versus phosphor field for the ZnS:Mn ACTFEL device at 300 K and 56 K. The luminescence is about the same for room temperature and low temperature operation; only at phosphor fields above 2 MV/cm a slight increase in luminescence is found for the low temperature operation.

Figure 5.3 shows the impact excitation efficiency versus phosphor field plot for the ZnS:Mn ACTFEL device at 300 K and 52 K operation. The impact excitation efficiency curve follows essentially the same trend for both room and low temperature device operation. The trend is, however, shifted to lower fields by about 0.3 MV/cm for the low temperature operation. The onset of the impact excitation efficiency at low temperature is around 0.5 MV/cm and at room temperature around 0.8 MV/cm. If the threshold is taken to be the intercept of the linear portion of the

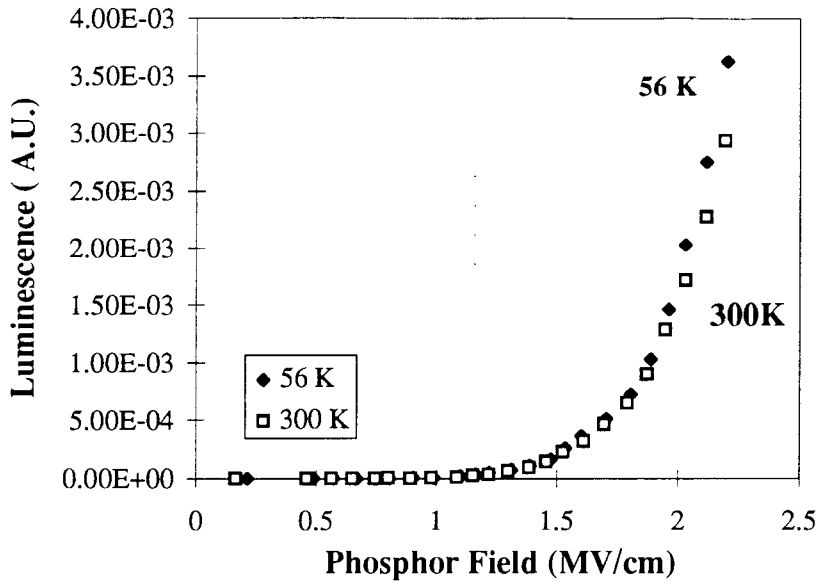

FIGURE 5.2. Luminescence versus phosphor field for a ZnS:Mn ACTFEL device ($V_{pre} = 178V$).

impact excitation efficiency plot, then the threshold for low temperature operation is around 1 MV/cm and for room temperature is around 1.3 MV/cm. There is no evidence for saturation found for room temperature operation below 2.2 MV/cm. However, the low temperature result shows evidence for the onset of saturation at around 2.1 MV/cm.

The higher impact excitation efficiency at 52 K is attributed to a hotter electron distribution in the phosphor. However, it is not excluded that a decrease of nonradiative transitions at 52 K may as well contribute to the higher conversion efficiency. The onset of saturation suggests that heating of the electron distribution is less efficient above above 2 MV/cm. This observation is consistent with the onset of impact ionization in the phosphor and is inconsistent with an increase in charge

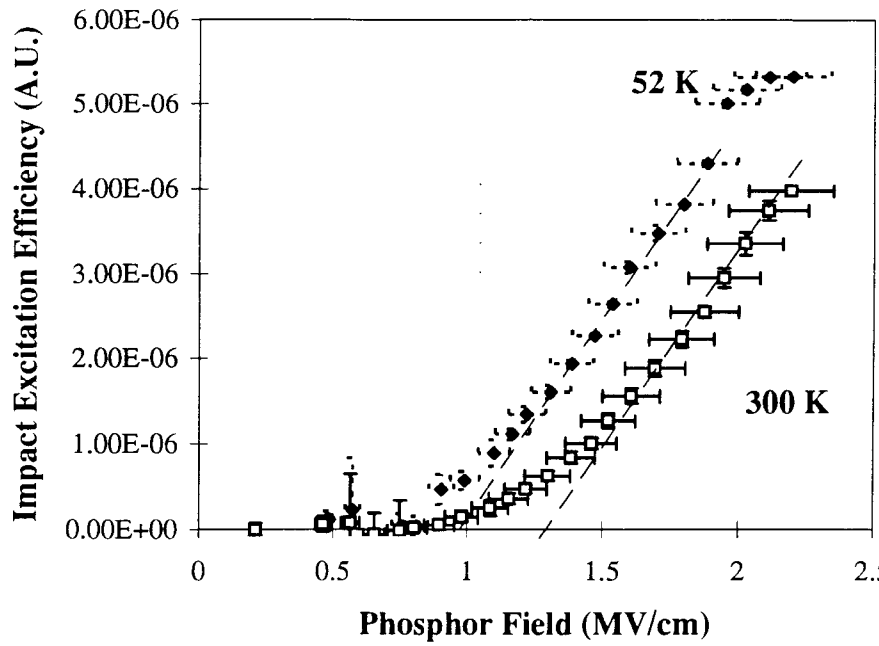

FIGURE 5.3. Impact excitation efficiency for a ZnS:Mn ACTFEL device at 300 K and 52 K (V_{pre} = 178V).

production through pure tunnel injection, since tunnel injection is temperature independent. Since previous research does not show any space charge generation in evaporated ZnS:Mn ACTFEL devices [25], the increasing slope in the conduction charge above 2 MV/cm, as shown in Fig. 5.1, is attributed to band-to-band impact ionization in the ZnS phosphor. Above the onset of band-to-band impact ionization, further heating of the electron distribution is inhibited since additional energy gained from the field is dissipated in the band-to-band impact ionization process. This assertion is supported by the Monte Carlo high-field transport simulation results of Pennathur [17]. The results of his high-field transport modeling suggest that the electron distribution does not significantly heat any further when band-to-band impact ionization is initiated.

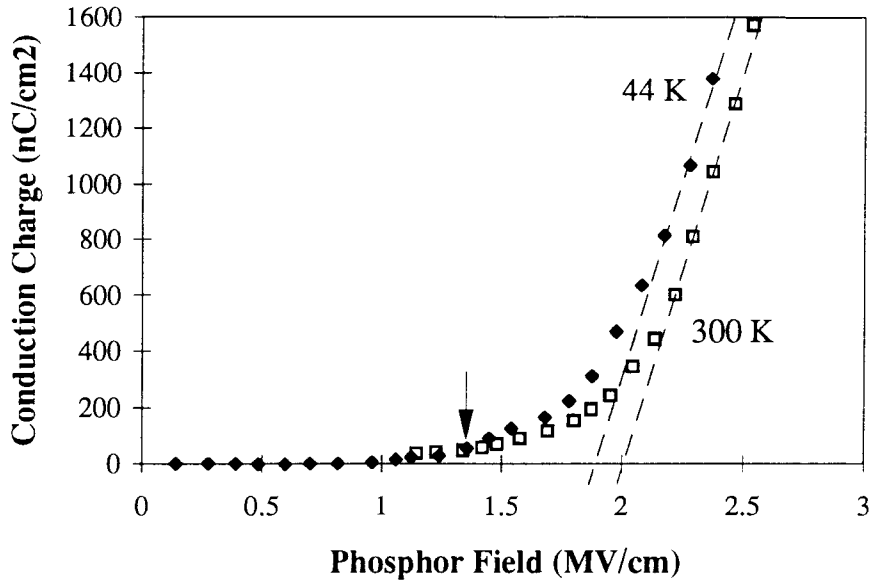

FIGURE 5.4. Conduction charge versus phosphor field for a $CaSrGa_2S_4$: Ce ACTFEL device at 300 K and 44 K (V_{pre} = 185V).

5.2. Impact Excitation Efficiency Measurements of $CaSrGa_2S_4$: Ce ACTFEL devices

Figures 5.4-5.9 show results for the $CaSrGa_2S_4$: Ce ACTFEL device. The conduction charge and the excitation efficiency in these figures is assessed using the measured device capacitances, as listed in Table (4.1). The impact excitation efficiency measurement for the $CaSrGa_2S_4$: Ce ACTFEL device is also conducted for the calculated insulator capacitance value of the device. That is the field-control circuit is calibrated for this insulator capacitance value and the calculations are performed with that value. The same qualitative trends are found if the calculated insulator capacitance is employed instead of the measured insulator capacitance.

Figure 5.4 shows the conduction charge versus phosphor field for the $CaSrGa_2S_4$: Ce ACTFEL device at room and low temperature operation. The operating parameters are: $V_{pre} = 185V$, $f = 60\,Hz$, $T = 0.6\,ms$. The charge transfer starts around 1 MV/cm at 44 K. The charge transfer at 300 K is not recorded to low enough fields to allow for an estimate of the onset of conduction charge, but from the graph is expected to start below 1 MV/cm. Only at phosphor fields below 1.4 MV/cm is slightly more conduction charge found for room temperature operation. Above 1.4 MV/cm, there is less conduction charge recorded for room temperature operation than for device operation at 44 K. For room temperature, the conduction charge increases strongly for a phosphor field above 2 MV/cm while this increase starts already at about 1.9 MV/cm at low temperature.

Phonon-assisted tunneling from the interface states does not seem to be an important electron sourcing mechanism for this device since the conduction charge curves show a weak temperature-dependence which is contrary to that expected for phonon-assisted tunneling. A transport-related process, however, is expected to be more efficient at low temperature due to reduced phonon scattering. Therefore, the increase in conduction charge above 2 MV/cm might be due to some transport-related process, such as charge multiplication, in the phosphor. This scenario is compatible with the observation of less conduction charge at room temperature.

Figure 5.5 shows the luminescence versus phosphor field for the $CaSrGa_2S_4$:Ce ACTFEL device at room temperature and low temperature operation. More luminescence is recorded for low temperature operation. Also, luminescence is already recorded for fields as low as 0.7 MV/cm for low temperature operation while for room temperature operation the luminescence is recorded only above 1.3 MV/cm.

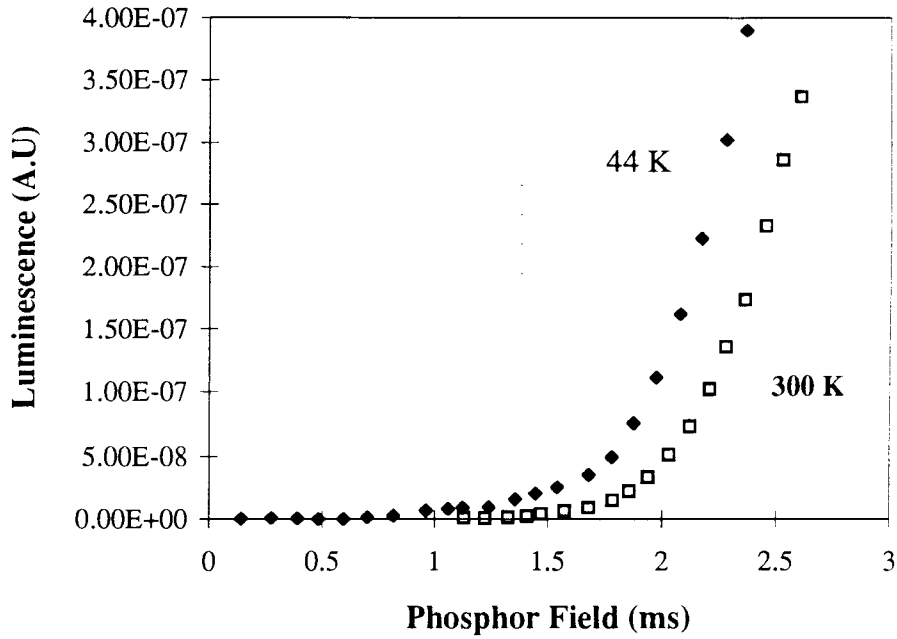

FIGURE 5.5. Luminescence versus phosphor field for a $CaSrGa_2S_4$:Ce ACTFEL device at 300 K and 44 K ($\lambda = 500\,\text{nm}$, $V_{pre} = 185\,\text{V}$).

Figure 5.6 shows the impact excitation efficiency versus phosphor field for the $CaSrGa_2S_4$: Ce ACTFEL device at room temperature. The impact excitation efficiencies for both cerium peak wavelengths are shown. The efficiencies for both wavelengths behave in essentially the same manner. The curves in Fig. 5.6 show three distinct ranges marked by its slope changes. Since the impact excitation efficiency is not recorded for fields lower than 1.1 MV/cm, it can only be assumed from the graphs that the onset of impact excitation lies below 1 MV/cm. If the threshold is taken to be the intercept of the straight line fit to the excitation efficiency, then a value of about 1.35 MV/cm is found for the threshold field. This value corresponds approximately to the value at which the conduction charge curves for both temperatures overlap in Fig. 5.4. This value marks the end of the first region. The

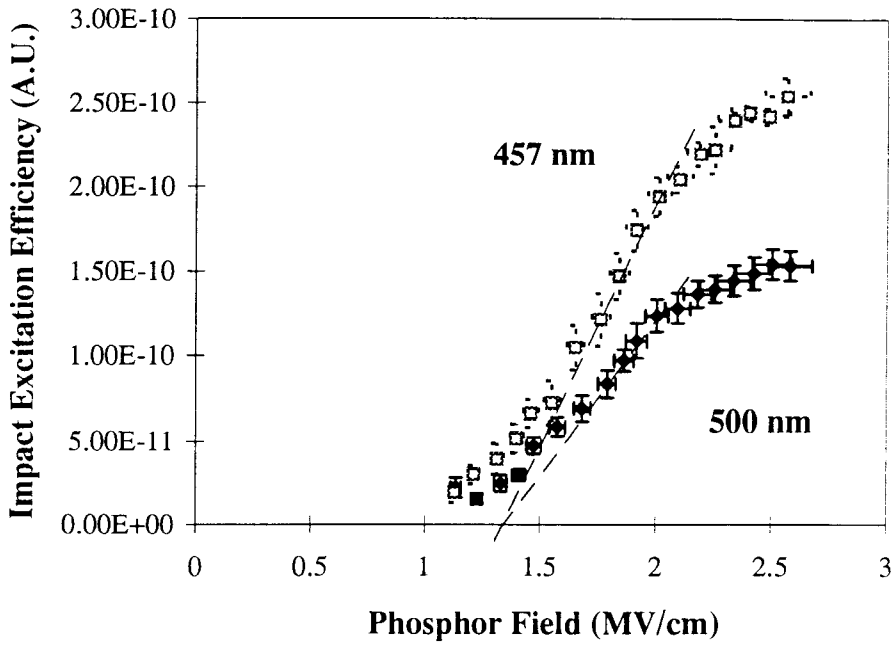

FIGURE 5.6. Impact excitation efficiency versus phosphor field for a $CaSrGa_2S_4$:Ce ACTFEL device at 300 K.

second region lies between 1.35 MV/cm and 1.9 MV/cm and has a steeper slope than the first region, indicating a significant amount of conduction charge flow. The third region starts at 1.9 MV/cm with the onset of saturation. A comparison of Figs. 5.4 and 5.6 indicates that saturation in the impact excitation efficiency occurs concomitantly with a rapid increase in conduction charge with the phosphor field.

Figure 5.7 shows the impact excitation efficiency versus phosphor field for the $CaSrGa_2S_4$: Ce ACTFEL device at 44 K. The excitation efficiencies for both cerium peak wavelengths are shown and both behave essentially in the same manner. The excitation efficiency increases at low and high fields. At low fields, the impact excitation efficiency peaks around 0.5 MV/cm for the major cerium peak (454 nm) and around 0.7 MV/cm for the minor emission peak of cerium (500 nm). This unexpected impact excitation efficiency peak is associated with a small, but measurable,

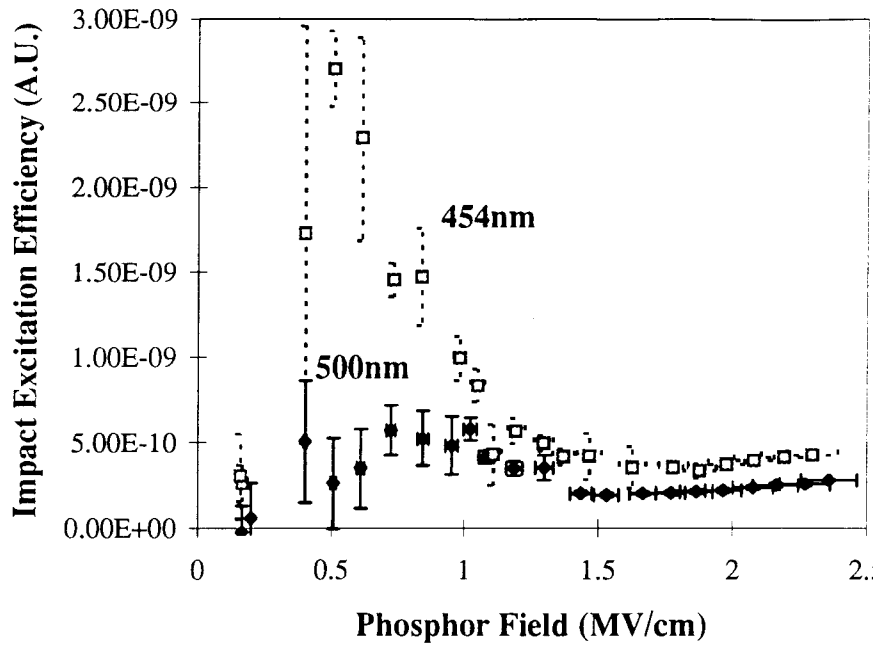

FIGURE 5.7. Impact excitation efficiency versus phosphor field for a $CaSrGa_2S_4$:Ce ACTFEL device at 44 K (500 nm) and 41 K (454 nm).

prethreshold luminescence that is detected prior to the onset of any measurable conduction charge. This leads to the assumption that the luminescence for phosphor fields of 0.5 to about 1.5 MV/cm is mostly due to some other mechanism than impact excitation.

The cause of this prethreshold luminescence is not yet understood. However, it is speculated that this prethreshold luminescence may be due to the ionization of cerium ions during the prepulse sequence. These ionized cerium ions could then radiatively recombine with the very first conduction electrons injected, even if they are injected at low fields. These captured electrons would not contribute significantly to the measured conduction charge since they drift only a short distance prior to

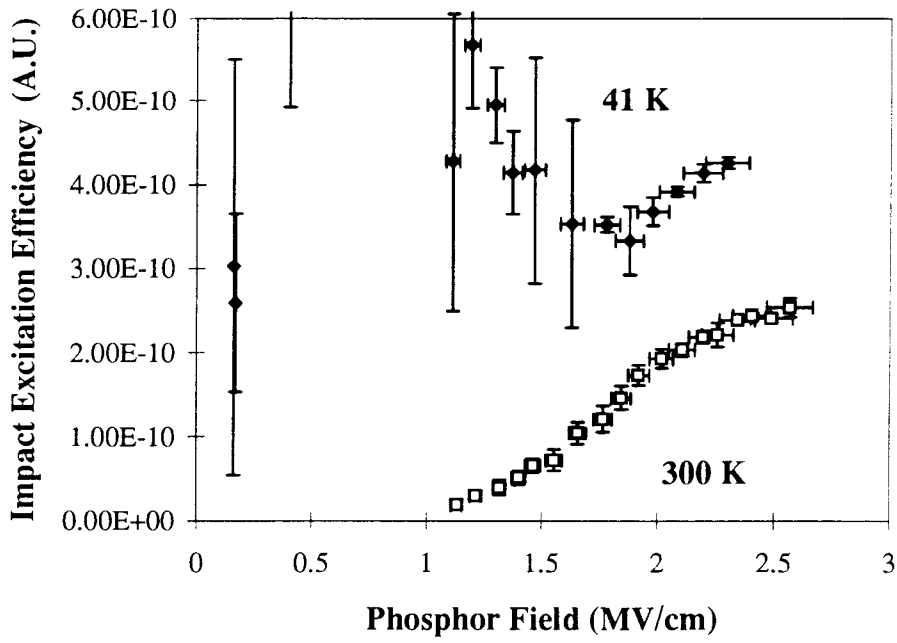

FIGURE 5.8. Impact excitation efficiency versus phosphor field for a $CaSrGa_2S_4$:Ce ACTFEL device for the main cerium peak at 41 K (454 nm) and 300 K (457 nm).

recombination. If a large fraction of the injected electrons recombine without drifting completely across the phosphor, the impact excitation efficiency could be very high.

This prethreshold luminescence was observed in two impact excitation efficiency experiments using a single ACTFEL device. Therefore, it is believed to be a real effect for this particular device. However, it remains to be determined whether the same effect can be observed in other $CaSrGa_2S_4$: Ce ACTFEL devices.

Figures 5.8 and 5.9 show the same excitation efficiency plots for the two emission peaks of cerium as shown in Fig. 5.7 and 5.6. But the high phosphor field portion of the curve is emphasised.

Figure 5.8 shows that the impact excitation efficiency of the device is almost two times higher at low temperature than at room temperature. No clear indication

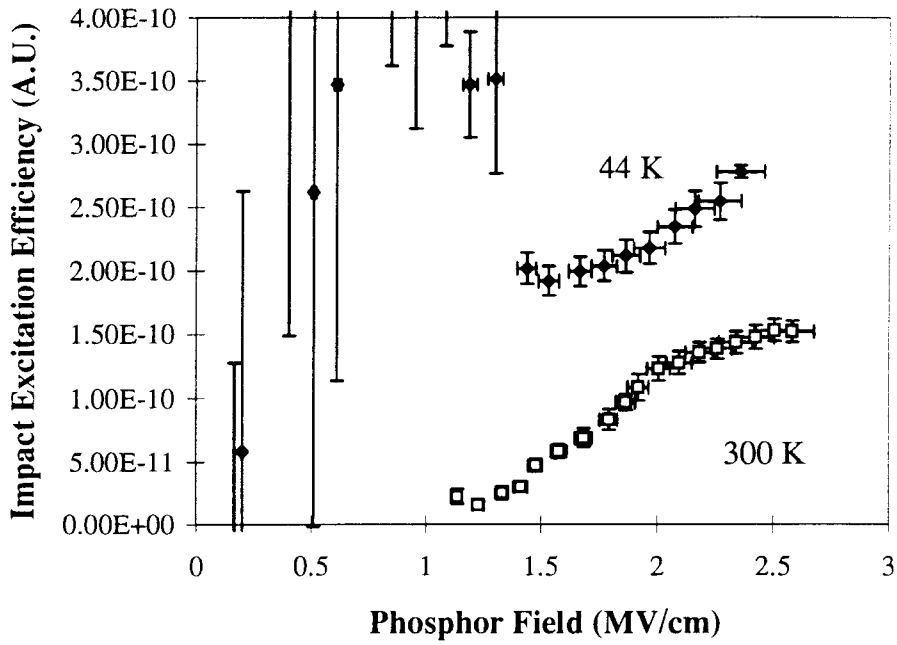

FIGURE 5.9. Impact excitation efficiency versus phosphor field for a $CaSrGa_2S_4$:Ce ACTFEL device for the minor cerium peak (500 nm) at 41 K and 300 K

of saturation is found at 41 K and no threshold field can be determined for the impact excitation efficiency at low temperature. However, it is believed that the low temperature curve would exhibit a threshold at $\sim$ 0.5 - 1 MV/cm if the prethreshold luminescence could be accurately corrected for.

The evidence found for interface state dominated charge supply in ZnS:Mn ACTFEL devices and for charge multiplication in the $CaSrGa_2S_4$: Ce ACTFEL device seem consistent with the results of the C-V studies of evaporated ZnS:Mn and $CaSrGa2S_4$: Ce by Long Pham [25]. He concluded that $CaSrGa_2S_4$: Ce ACTFEL devices possess a lower density of interface states which are deeper in energy and spread out over a broader range of energy.

5.3. Summary

Some evidence for phonon-assisted tunneling and band-to-band impact ionization at higher fields as a carrier injection mechanism for ZnS:Mn ACTFEL devices is found. The threshold values for the impact excitation for ZnS:Mn ACTFEL devices are 1MV/cm at 52K and 1.3 MV/cm at 300K. The saturation onset is found to be 2.1 MV/cm for device operation at 52K.

No evidence for significant phonon-assisted tunneling is found in the $CaSrGa_2S_4$: Ce ACTFEL device. However some evidence for charge multiplication in the bulk is found. The impact excitation efficiency threshold for room temperature operation is 1.4 MV/cm. The impact excitation efficiency saturates around 2.3 MV/cm.

6. CONCLUSIONS & RECOMMENDATIONS FOR FUTURE WORK

The objective of this thesis was to experimentally assess the impact excitation efficiency with respect to the phosphor field for two ACTFEL devices; evaporated ZnS:Mn and sputtered $CaSrGa_2S_4$: Ce.

The phosphor field is maintained constant during the measurement by means of a field-control circuit. Threshold values for the impact excitation efficiency of both types of ACTFEL devices could be estimated as 1 MV/cm at 52 K and 1.3 MV/cm at 300 K for the ZnS:Mn ACTFEL device and as 1.4 MV/cm for for room temperature operation of the $CaSrGa_2S_4$: Ce ACTFEL device. A threshold value for low temperature operation could only be found for the ZnS:Mn ACTFEL device, because the threshold of the $CaSrGa_2S_4$: Ce ACTFEL devices was masked by some prethreshold luminescence. The saturation onset is estimated to be 2.1 MV/cm for the ZnS:Mn device operated at 52K; for the $CaSrGa_2S_4$: Ce ACTFEL device it is estimated to be around 1.9 MV/cm for room temperature operation.

In the following recommendations for future work with regard to the field-control circuit, the driving waveform, and data processing for future measurements are made. In general, it is suggested that ACTFEL devices which allow a direct measurement of the insulator capacitance be used. For example, if an ACTFEL stack is prepared so that a stack without a phosphor is present on the same test glass as the ACTFEL device, the insulator capacitance could be experimentally determined. Devices fabricated in such a manner may allow for a more accurate calibration of the field-control circuit. An evaluation of the leakage charge with respect to the polarization phosphor field may allow the evaluation of the depth

and density of the interface states which thus, would allow a discrimination of the transport from the interface state processes.

Further impact excitation efficiency measurements using other $CaSrGa_2S_4$:Ce ACTFEL devices should be undertaken to determine whether the prethreshold luminescence is peculiar to the single device investigated or if it is representative of thiogallate devices. If it is found to be characteristic of thiogallate ACTFEL devices, the origin of the prethreshold luminescence needs to be further investigated. If the prethreshold luminescence is due to ionization processes occurring during the prepulse sequence, then measurements using bipolar field-control pulses may eliminate the prethreshold luminescence and allow for an artifact-free measurement of the impact excitation efficiency.

The measurements for the ZnS:Mn ACTFEL device could be repeated/confirmed using new ACTFEL devices since the layer thicknesses were not well established for the device employed in this study. Thus, if the layer thicknesses are known to a higher degree of precision, the phosphor field could be determined with more precision.

Additionally, the impact excitation efficiency measurement should be performed using a ZnS:Tb ACTFEL device. This type of device was evaluated previously by Streicher et al. [5]. However the experimental procedure for conducting the impact excitation efficiency experiment has been modified substantially in the work described herein and, therefore, the ZnS:Tb ACTFEL device measurement should be reconfirmed.

The phosphor field is controlled by means of a field-control circuit during the measurement of the impact excitation efficiency. The performance of this circuit could be improved. A faster high voltage amplifier and differential amplifier may be able to reduce the feedback time of the field-control circuit and, thus, oscillations

in the measured charge transients as well as in the phosphor field transients. A faster field-control circuit would not only allow for a more precise regulation of the phosphor field but also for driving the device to higher fields. The present field-control circuit implementation has difficulties keeping up with the high charge flow at high fields.

The driving waveform used for the impact excitation efficiency experiment is rather complex and consists of three parts; a prepulse sequence, a field-control pulse, and a dead time in between. The parameters used for each part of the waveform have some influence on the measured impact excitation efficiency. More work is required to determine the suitability of the presently used waveform or of an alternative waveform. The dependence of the impact excitation efficiency measurement on the length and voltage amplitude of the prepulse sequence, as well as the time delay after the prepulse sequence, need to be investigated in further detail; i.e., the influence of the polarization charge due to the prepulse sequence on the impact excitation efficiency needs to be investigated.

A modified version of the field-control circuit with bipolar field-control pulses could obviate the need for prepulses. The tunability of the phosphor field by means of the arbitrary waveform generator and a differential amplifier is currently being investigated by Patrick James and the author. Preliminary experiments show that the basic circuit works as expected; however, fine tuning of the phosphor field pulse may be a challenge. The results of impact excitation efficiency measurements obtained by means of the use of a prepulse sequence and by means of the use of bipolar field-control pulses should be compared in order to determine which approach leads to a more reliable estimate of the impact excitation efficiency.

The impact excitation efficiency data is currently processed by means of an EXCEL Macro written in Visual Basic. Internal and external charge, phosphor field,

the luminescent transient curves as well as charge versus voltage, and charge versus phosphor field curves are generated via the macro from the raw data acquired. The conduction charge, integrated luminescence, and impact excitation efficiency are also plotted versus phosphor field. This means processing data is relatively slow and required RAM memory of at least 16 Mega Bytes and a substantial amount of memory for the storage of the processed information. Thus, the impact excitation efficiency data processing needs further simplification. The transients are generated for the verification of the validity of the final data, i.e. the correct assessment of the conduction charge, the phosphor field, and the luminescence. It would be possible, after some restructuring of the data processing, to delete those graphs after the verification of the final data and to reduce the required memory. The development of a Visual Basics program instead of the EXCEL macro, might save processing time.

BIBLIOGRAPHY

[1] Y.A. Ono, *Electroluminescent Displays*, Worlds Scientific publishing Co. Ltd., Singapore, 1995.

[2] D.C. Krupka, "Hot-Electron Impact Excitation of Tb^{3+} Luminescence in ZnS : Tb^{3+} Thin Films", *J. Appl. Phys.*, vol. 43, no. 2, pp. 476-481, (1972).

[3] K.Streicher, T.K.Plant, and J.F. Wager, "Hot-electron impact excitation of ZnS:Tb alternating-current thin-film electroluminescent devices", *J. Appl. Phys.*, vol. 78, no. 3, pp. 2101-2104, (1995).

[4] A.A. Douglas, "Alternating-Current Thin-Film Electroluminescent Device Physics and Modeling", *MS Thesis, Oregon State University*, (1993).

[5] K.R. Streicher, "Electro-Optic Characterization of ZnS : Tb^{3+} ACTFEL Devices for Probing the Hot Electron Distribution", *MS Thesis, Oregon State University*, (1994).

[6] E. Bringuier, "Charge transfer in ZnS-type electroluminescence", *J. Appl. Phys.* vol. 66, no. 3, pp. 1314-1325, (1989).

[7] S. Kobayashi, J.F. Wager, and A. Abu-Dayah, "Distribution of Trapped Electrons at Interface States in ACTFEL Devices;Electroluminescence", *Proceedings of the Sixth International Workshop on Electroluminscence*, Cinco Puntos Press, El Paso, (1992).

[8] E. Bringuier, "Tentative anatomy of ZnS-type electroluminescence", *J. Appl. Phys.* vol. 75, no. 9, pp. 4291-4312, (1994).

[9] W.M. Ang, S. Pennathur, L. Pham, J.F. Wager, S.M. Goodnick, A. A. Douglas "Evidence for band-to-band impact ionization in evaporated ZnS:Mn alternatin-current thin-film electroluminescent devices", *J. Appl. Phys.* , vol. 77 , no. 6, pp. 2719-2724, (1995).

[10] A.I. Abu-Dayah, "Internal Charge-Phosphor Field Analysis, Electrical Characterization, and Aging Studies of AC Thin-Film Electroluminescent Devices", *MS Thesis, Oregon State University*, (1993)

[11] R.L. Thuemler,P.D. Keir, J.F. Wager, "Phosphor field Dependence in ALE-Grown SrS:Ce ACTFEL Devices", *SID 95 Digest*, pp. 473-475, (1993).

[12] K. Brennan, "Theory of high-field electronic transport in bulk ZnS and ZnSe", *J. Appl. Phys.* vol. 64, no. 8, pp. 4024-4030, (1988).

[13] H.-J. Fitting, A. von Czarnowski, G.O. Mueller, "Ballistic Transport in alkaline Earth Sulfides", *J. Crystal Growth*, vol.'101, pp. 876-881, (1990).

[14] R. Mach and G.O. Mueller, "Ballistic Transport and Electroluminescence in IIB-VI Compounds", *J. Crystal Growth* vol. 101, pp. 967-975, (1990).

[15] K. Bhattacharyya, S.M. Goodnick, and J.F. Wager, "Monte Carlo simulation of electron transport in alternating-current thin-film electroluminescent devices", *J. Appl. Phys.* vol. 73, no. 7, pp. 3390-3395, (1993).

[16] S.S. Pennathur, K. Bhattacharry, J.F. Wager, and Stephen M. Goodnick, "Full-band Ensemble Monte Carlo Modeling of High Field Transport in the ZnS Phosphor of AC Thin Film Electroluminescent Devices", *Proceedings of the third international Workshop on Computional Electronics*, (1994).

[17] S.S. Pennathur, "Monte Carlo Device Modeling, Applications on Parallel Computers", *PhD Thesis, Oregon State University*, (1995).

[18] G.O. Mueller, R. Mach, "Efficiency and Saturation in AC Thin Film Structures", *Physica Status Solidi*, vol. A 81, pp. 609-623, (1984).

[19] E. Bringuier and K. Bhattacharyya, "Hot-electron-impact cross section of deep impurities in semiconductors", *unpublished.*

[20] G. Blasse, B.C. Grabmaier, *Luminescent Materials*, Springer-Verlag, Berlin Heidelberg, (1994).

[21] N. Yamashita and Y. Michitsuji, "Photoluminscence Spectra and Vibrational Structures of the SrS : Ce^{3+} and SrSe : Ce^{3+} Phosphors" *J. Electrochem. Soc.: Solid-State Science and Technology* vol. 134, no. 11, pp. 2932-2934, (1987)

[22] J. David Irwin, *Basic Circuit Analysis 2nd Edition*, pp. 170, (1987).

[23] R. Mach and G.O. Mueller, "Ballistic Transport and Electroluminescence in IIB-VI and IIA-VI Combounds, *J. Crystal Growth* vol. 101, pp. 967-975, ().

[24] *Photo Multiplier Tubes*, Hamamatsu, Manual, (1988).

[25] L.V. Pham, J.F. Wager, S.S Sun, E. Dickey, R.T. Tuenge, C.N. King "Electrical characterization of blue electroluminescent devices" SPIE vol. 2174, pp 190-199, (1994).